solids

MDPI

Review

Ceramic Additive Manufacturing via Vat Photopolymerization and Extrusion Processes: A Comprehensive Review of Processing Strategies

Soufyane Satha *, Mohamed Aymen Ben Achour, Mohamed Rguiti, Yannick Lorgouilloux, Florian Jean and Christian Courtois

CERAMATHS—Laboratoire de Matériaux Céramiques et de Mathématiques, INSA Hauts-de-France, University Polytechnique Hauts-de-France, F-59313 Valenciennes, France
* Correspondence: soufyane.satha@uphf.fr; Tel.: +33-782943269

Abstract

Additive manufacturing (AM) techniques are continuously evolving to meet the increasing demand for high-performance ceramics with intricate geometries. This review covers four widely investigated ceramic AM methods: stereolithography (SLA), digital light processing (DLP), fused deposition modeling (FDM), and direct ink writing (DIW). Each technique is analyzed from a technical standpoint, with particular attention given to feedstock formulation, printing parameters, debinding, sintering, and final densification. Vat photopolymerization provides high resolution and good surface quality, but remains constrained by photocurable slurry behavior. FDM offers accessible equipment and material versatility, though high ceramic loading can lead to feeding and printing difficulties. DIW can process highly loaded ceramic inks and is suitable for porous and architectured structures, but requires precise control of ink rheology and shape retention. The main challenges associated with ceramic printing are also examined, together with proposed solutions, emerging trends, and research gaps. This review provides a comparative overview of the critical parameters governing ceramic AM and helps identify the most suitable technique according to the targeted application.

Keywords: additive manufacturing; ceramics; printing parameters; fused deposition modeling; vat photopolymerization; extrusion techniques; direct ink writing; stereolithography; digital light processing

Check for updates

Academic Editor: Juan B. Carda Castelló

Received: 4 August 2026
Revised: 24 September 2026
Accepted: 8 October 2026
Published: 2 November 2026

Copyright: © 2026 by the authors. Licensee MDPI, Basel, Switzerland. This article is an open access article distributed under the terms and conditions of the Creative Commons Attribution (CC BY) license.

1. Introduction

As engineering and technological advancements continue to accelerate, two sectors are likely to strongly influence the development of innovative materials and manufacturing techniques: healthcare and sustainable technologies. The ability to fabricate advanced functional parts, such as custom-designed prosthetics tailored to an individual's biomechanics [1,2] or architected materials for future energy harvesting and storage [3,4], is becoming a practical reality rather than a distant ambition.

Additive manufacturing (AM), commonly known as 3D printing, is transforming the production of complex parts. Unlike traditional subtractive methods, such as machining, which remove material from a solid block, AM builds structures layer by layer from digital models. This process significantly decreases material waste and offers advantages such as design flexibility, faster production times, and better resource efficiency [5].

Unlike conventional techniques such as injection molding, AM enables rapid prototyping of intricate geometries. Injection molding involves melting materials and injecting them into preformed molds, but producing these molds is often costly and time-consuming. While conventional methods still dominate in high-volume production, AM offers a highly effective solution for low- to medium-production runs where design freedom is essential [6,7].

The history of AM dates to the 1980s, with the development of stereolithography (SLA) and selective laser sintering (SLS). Over the past decade, the field has expanded significantly, offering a wide range of techniques for a variety of materials and applications. Today, seven primary AM categories are recognized: vat photopolymerization (e.g., SLA and digital light processing (DLP)), powder-bed fusion (e.g., SLS, selective laser melting (SLM), direct metal laser sintering (DMLS), and electron beam melting (EBM)), material extrusion (e.g., fused deposition modeling (FDM) and direct ink writing (DIW)), material jetting (e.g., PolyJet, MultiJet Printing (MJP)), binder jetting, sheet lamination (e.g., laminated object manufacturing (LOM) and ultrasonic additive manufacturing (UAM)), and directed energy deposition (e.g., laser-engineered net shaping (LENS) and electron beam additive manufacturing (EBAM)) [8].

These methods employ photopolymerization, laser melting, and material extrusion to produce components with varied properties from polymers, metals, ceramics, and composites.

Today, ceramics are one of the most widely used classes of materials in aerospace, electronics, and biomedical engineering [9–11] due to their high thermal stability, hardness, corrosion resistance, and functional properties.

Among the different ceramic AM processes, vat photopolymerization and extrusion-based techniques are among the most widely investigated. Vat photopolymerization, including SLA and DLP, is based on the selective curing of a ceramic-loaded photocurable resin to solidify successive layers. Extrusion-based processes include FDM, in which a ceramic-loaded thermoplastic filament is deposited through a heated nozzle, and DIW, in which ceramic pastes, gels, or slurries are directly extruded. Regardless of the shaping technique, fabricating ceramic parts requires subsequent debinding and sintering steps. Debinding removes the organic binder, often through solvent debinding to create open porosity followed by thermal debinding, reducing the risk of defects such as cracking or blistering [12,13]. Sintering then applies high-temperature treatment to densify the material and achieve its final mechanical and functional properties. Although these techniques share the objective of fabricating complex ceramic structures, they involve different optical, rheological, mechanical, and thermal constraints.

Several reviews have already discussed ceramic additive manufacturing, either by focusing on individual techniques, specific ceramic materials, or particular application fields [14–19]. However, direct comparisons between vat photopolymerization and extrusion-based processes remain limited, particularly regarding the relationships between material formulation, ceramic loading, photopolymerization or rheological requirements, printing parameters, debinding, sintering, densification, and scalability. Comparing these parameters is essential because improvements in one aspect, such as resolution or ceramic loading, may negatively affect another aspect, such as viscosity, curing depth, filament flexibility, drying behavior, or dimensional accuracy.

This review presents an overview of vat photopolymerization methods, including SLA and DLP, and extrusion-based techniques, including FDM and DIW, from a technical standpoint. The main process and printing parameters, common challenges encountered during ceramic printing, and technical approaches proposed to overcome them are analyzed. Particular attention is given to photopolymerization mechanisms, slurry formulation, filament fabrication, rheological behavior, debinding, sintering, and final densification. Powder-bed

fusion using a laser beam (PBF-LB), Multi Jet Fusion (MJF), and binder jetting are excluded because they involve powder-bed preparation and consolidation mechanisms that require a separate comparative framework. As these processes depend on aspects such as powder flowability and packing density, reviewing these parameters would extend the scope of the review beyond the intended focused comparison of vat photopolymerization and extrusion-based processes. Representative ceramic-based applications and current research trends are also discussed with an emphasis on oxide-based ceramics. Carbides, nitrides, and borides are not comprehensively covered, as this review is focused on processing–property relationships rather than attempting an exhaustive survey of all ceramic compositions. Finally, the four techniques are directly compared in terms of ceramic loading, resolution, feedstock requirements, post-processing constraints, achievable density, cost, versatility, and scalability. This cross-process comparison aims to identify the most suitable applications for each technique and provide valuable insights that complement existing reviews.

2. Literature Review Methodology

The literature reviewed in this work was primarily identified through Google Scholar searches, with the last search conducted in 2026. The strategy used a combination of keywords related to three main areas: general additive manufacturing, such as "3D printing" and "ceramic additive manufacturing"; specific techniques, including "vat photopolymerization", "stereolithography", "digital light processing", "fused deposition modelling", and "direct ink writing"; and formulation and processing parameters, such as "photoinitiators", "ink rheology", and "filament fabrication". No fixed starting year was used for the search. Recent articles from approximately the preceding 10–15 years were prioritized, while older publications were also considered when they provided important fundamental information. Research and review papers published in peer-reviewed journals were the main sources used. Book chapters and full-length conference papers were also considered when they provided relevant information for the technical discussion. Conference abstracts, patents, and dissertations were not included in the reviewed literature.

Publications were selected based on their relevance to the different aspects analyzed for each technique, including processing and fabrication strategies, material formulation, printing limitations, and ceramic-based applications. For quantitative comparisons, attention was given to the reported material composition, ceramic solid loading, processing conditions, and measurement methods to assess whether the results could be meaningfully compared.

This review focuses on SLA, DLP, FDM, and DIW. The reasons for excluding powder-bed processes, including PBF-LB, MJF, and binder jetting, are explained in the Introduction. The selected literature was organized so that the reader can first understand the main parameters of each technique, followed by its advantages and limitations, ceramic-based applications, and the approaches used to address processing difficulties. Finally, the four techniques were compared in terms of their feedstock requirements, printing parameters, post-processing, and final properties.

3. Main Techniques of Additive Manufacturing

3.1. Vat Photopolymerization

This section begins with an overview of vat photopolymerization technology. We first analyze the stereolithography method, explaining its principles, process parameters, different types of photo-initiators, and the fundamental photopolymerization mechanisms. A comparison between digital light processing (DLP) and stereolithography (SLA) is then provided, highlighting their main differences. Finally, we discuss ceramic-based

applications of vat photopolymerization, focusing on significant challenges reported in the literature and the proposed solutions.

3.1.1. Stereolithography (SLA)

Principle

Stereolithography (SLA) is an additive manufacturing technique based on photopolymerization, in which a photocurable resin is mixed with inorganic fillers, such as ceramics, to form a slurry. The latter is held in a vat and irradiated with ultraviolet (UV) light directed by galvanometers (Galvo mirrors) from a laser source to selectively cure and solidify specific regions. Figure 1 shows the classic stereolithography setup. After each layer is cured, the build platform either moves upward (top-down) or downward (bottom-up) to allow the next layer to be cured [19]. This process continues layer by layer until the complete object is formed [14].

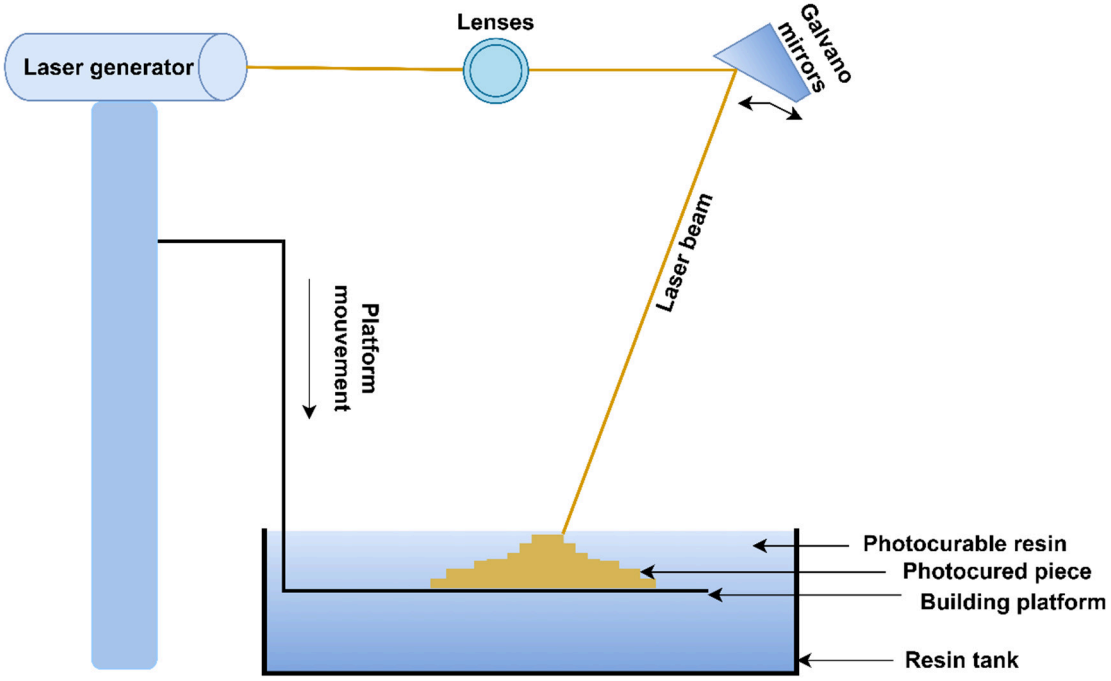


Figure 1. Stereolithography principle.

The printed parts are usually rinsed with a solvent such as isopropyl alcohol (IPA) for several minutes to remove uncured material and are then post-cured with UV light to enhance their mechanical and elastic properties [20]. The photocurable resin typically consists of monomers, oligomers, UV initiators, and stabilizers. Additives such as surfactants are often included to promote deagglomeration and ensure a homogeneous dispersion [21].

Photopolymerization Types

Different classes of photoinitiators can be used depending on the targeted polymerization mechanism. The most common include Type I and Type II free-radical photoinitiators, cationic photoinitiators, visible-light photoinitiators, and hybrid initiators. These systems are summarized in the following subsections.

Free Radical Photopolymerization

Free radical photopolymerization involves generating free radicals through the decomposition of a photoinitiator when exposed to light. Two types of photoinitiators are commonly involved in this process.

Type I photoinitiators are widely used due to their high efficiency in initiating polymerization. They undergo homolytic bond cleavage when exposed to light, generating two reactive radicals that readily interact with monomers and oligomers to initiate chain growth [22]. Common examples include benzoin ethers, acylphosphine oxides, α-hydroxy ketones, and α-amino ketones.

Type II photoinitiators operate via a hydrogen-abstraction mechanism. Upon absorbing light, molecules such as benzophenone or thioxanthone reach an excited state and interact with a co-initiator, typically an amine, which donates a hydrogen atom. This results in the formation of two reactive radicals, one on the photoinitiator and the other on the co-initiator, which then initiate the polymerization process [22].

The efficiency of a photoinitiator depends on three main factors: its radiation absorption efficiency, the rate of radical generation, and the reactivity of the resulting radicals [22].

Cationic Photopolymerization

Cationic photopolymerization involves the decomposition of cationic photoinitiators, such as diaryliodonium salts and triarylsulfonium salts, under UV irradiation. This produces a positively charged species that reacts with a monomer to form a cationic center, which then propagates by reacting with subsequent monomers [22]. The polymerization continues until a nucleophile neutralizes the cationic chain.

One significant advantage of cationic photopolymerization is its resistance to oxygen inhibition. Unlike free radical systems, where oxygen scavenges radicals and hinders polymerization, cationic species are not significantly affected by oxygen [23]. As a result, cationic systems often yield more uniform, defect-free materials. Additionally, these reactions do not require inert gas environments, thereby lowering processing costs [23].

Moreover, cationic systems often rely on less irritating monomers, such as epoxides, in contrast to the acrylates and methacrylates typically used in free radical systems [24]. Furthermore, this technique reduces volumetric shrinkage by using cyclic monomers. These monomers undergo ring-opening polymerization, as illustrated in Figure 2, resulting in minimal volumetric change compared to linear acrylates and methacrylates [25].

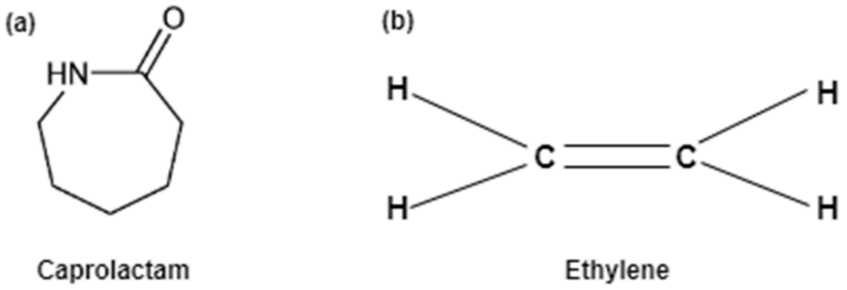


Figure 2. Examples of monomers: (**a**) cyclic monomer and (**b**) linear monomer.

Another key difference is the "dark curing phenomenon", in which polymerization continues even after light exposure ends. This effect is enhanced by thermal treatment [26], resulting in more thorough polymerization and improved mechanical properties. However, dark curing makes it harder to control the extent of polymerization, as the reaction may continue after the light source is turned off.

Additional drawbacks include moisture sensitivity, as water can terminate cationic chains by forming hydroxyl groups or alcohols [27] and the potential for chain transfer reactions that alter polymer molecular weight and properties. Moreover, cationic photopolymerization tends to be slower than free-radical polymerization due to its lower reactivity.

Hybrid Photopolymerization

To overcome the limitations of both free-radical and cationic polymerization, hybrid photopolymerization systems have been developed. These systems combine two polymerization mechanisms, typically a cationic and a free-radical process, by using two types of monomers and two corresponding photoinitiators.

Each photoinitiator independently initiates polymerization in its respective system (e.g., an acid for cationic polymerization and an acrylate for radical polymerization). The concurrent growth of both polymer chains leads to crosslinking, resulting in a solidified material.

A second type of hybrid photopolymerization involves the use of hybrid monomers that a single photoinitiator (either cationic or free-radical) can activate. These monomers contain functional groups and structural features that enable them to participate in both polymerization mechanisms. For example, Bednarczyk et al. (2021) [28] studied the synthesis of hybrid coatings using epoxy acrylate monomers. They combined diaryliodonium and triarylsulfonium cations for cationic polymerization with α-hydroxyketones and acylphosphine oxides for free-radical initiation, thereby achieving improved hardness, adhesion, and reduced curing times. Nowak et al. (2017) [29] evaluated various photoinitiators for hybrid monomers. For cationic polymerization, they tested Sylanto 7M-S, Sylanto 7M-P, Speedcure 938, Irgacure 250, diphenyliodonium hexafluorophosphate (HIP), and Esacure 1187. For free radical polymerization, Irgacure 184, Irgacure 127, Irgacure 651, Irgacure 907, Irgacure 819, and diphenyl (2,4,6-trimethylbenzoyl) phosphine oxide (TPO, marketed as Speedcure TPO) were used. Their results showed that Sylanto photoinitiators were more effective in cationic systems due to intense UV absorption at 320 nm and 365 nm. Meanwhile, Irgacure 819 and Speedcure TPO demonstrated superior performance in free-radical polymerization.

Thus, the performance of a photoinitiator is dictated by its absorption profile, the efficiency of radical or cation generation, and the reactivity of the generated species [27]. The advantages and drawbacks of each photopolymerization type are summarized in Table 1.

Table 1. Advantages and drawbacks of different types of photopolymerization.

Type of Photopolymerization	Advantages	Drawbacks
Free radical photopolymerization	High reactivity of photo-initiators Fast polymerization	Oxygen inhibition Limited depth penetration
Cationic photopolymerization	Less irritating and less toxic monomers Dark polymerization	Moisture inhibition Slower polymerization
Hybrid photopolymerization	Better mechanical properties Combined advantages of both free radical and cationic photopolymerization	Difficulty in controlling the photopolymerization Complex system

Influence of Process Parameters

Several key factors affect the printing quality of the final parts produced via vat photopolymerization. These include the type and concentration of the photoinitiator, the

type and amount of filler, dispersant additives, and curing conditions such as wavelength, exposure duration, and temperature.

Influence of Temperature and Additive Content

It is well known that increasing the curing temperature accelerates polymerization and improves mechanical properties. This is due to the enhanced mobility of free radicals on polymer chains caused by higher temperatures, making them more likely to react with double bonds rather than other radicals, thereby promoting more complete polymerization. Additionally, extending UV exposure time also enhances mechanical performance by ensuring complete polymerization.

The type and quantity of photoinitiators largely depend on the type of filler and monomer. A low concentration of photoinitiator can result in a shallow curing depth. In contrast, excessive amounts can quickly absorb large amounts of UV light on their surface, accelerating their decay. The high concentration of free radicals leads to chain termination reactions between the radicals and acrylic macromolecules, or to a loss of reactivity due to radical recombination. Both scenarios can reduce the cure depth [30].

This phenomenon was experienced by several researchers, such as Liu et al. (2022) [30], who examined how TPO content affects formulations containing O-phenylphenoxyethyl acrylate (OPPEOA), 1,6-hexanediol diacrylate (HDDA), tripropylene glycol diacrylate (TPGDA), and ethoxylated trimethylolpropane triacrylate, using $BaTiO_3$ as a ceramic filler. They discovered that 3 wt% TPO provided the highest cure depth, whereas higher concentrations reduced it.

He et al. (2022) [31] reported similar findings for barium calcium zirconate titanate (BCZT) ceramics processed via DLP using the same monomer mixture and photoinitiator. Their results confirmed that 3 wt% TPO was optimal and higher concentrations did not provide any meaningful enhancement.

Furthermore, cure depth also depends on the applied energy dose following Jacobs' formula [32,33] presented in Equation (1).

$$C_d = D_p \, ln\left(\frac{E}{Ec}\right) \quad (1)$$

where

Cd is the curing depth (μm);

Dp is the attenuation length (μm);

E is the applied energy dose (mJ/cm^2);

Ec is the critical energy dose (mJ/cm^2).

The attenuation length (D_p) and critical energy dose (E_c) are obtained directly from the slope and intercept of the C_d vs. ln(E) plot. Thus, this mathematical equation bridges slurry optics and photopolymerization kinetics with dimensional accuracy, serving as a fundamental tool for tailoring exposure parameters. By optimizing the E/Ec ratio, one can maintain a precisely calculated curing depth, ensuring an optimal curing step and overall printing accuracy.

Moreover, the curing depth varies significantly with filler composition. For example, Liu et al. (2024) [34] explored DLP printing of $BaTiO_3$ doped with Sn (2–13 mol%) and found that 2 wt% TPO with 50 mJ/cm^2 was optimal for 6 mol% Sn. However, due to changes in refractive index and density at different Sn levels (2, 11, 13 mol%), the same dose was insufficient, requiring an increase to 100 mJ/cm^2 to achieve the desired cure depth. While higher energy can increase depth, it must be kept sufficiently low to maintain accuracy.

Furthermore, deeper curing is not always better. Li et al. (2024) [35] found that an excessive curing depth decreased monomer conversion (from 5.2% to 2.0%), resulting in internal stress and potentially weakened green parts.

Another essential parameter is dispersant content, which reduces resin viscosity and stabilizes particle dispersion, thus producing a fluid slurry even at high filler content, which ensures successful and uniform printing. The optimal dispersant level depends on the filler type, size, and concentration. Heavily loaded or nano-filled resins need higher dispersant levels to prevent sedimentation.

For instance, Pan et al. (2023) [36] studied potassium sodium niobate (KNN) ceramics prepared via DLP and found that the resin viscosity was lowest at 5 wt% Solsperse 41000 and increased at 6 wt%. This increase can be caused by exceeding the adsorption limit of the ceramic particles, which can leave some free dispersant molecules that may cause flocculation, thus enhancing viscosity.

Similarly, Liu et al. (2022) [30] and He et al. (2022) [31] identified optimal viscosities for $BaTiO_3$ and BCZT ceramics at 1.5 wt% and 1 wt% dispersant concentrations, respectively, with a 40 vol% ceramic loading.

Previous research has shown that 5 wt% dispersant is the optimal content for a specific ceramic type and content. However, caution is advised because, at and above this concentration, the dispersant content becomes significant when added to other organic additives and can negatively influence various parameters. For example, high organic content can complicate the debinding step, necessitating extended debinding times. Furthermore, a higher organic component results in lower ceramic loading, which can lead to increased shrinkage or even debinding failure if the ceramic loading is insufficient.

Overall, optimizing process parameters and additive contents in vat photopolymerization of ceramics requires a delicate balance. A compromise between ceramic loading, rheological behavior, and curing depth and accuracy must be found to ensure successful printing, defect-free debinding, and a high final relative density.

3.1.2. Digital Light Processing

Comparison with Stereolithography

This technique is similar to stereolithography (SLA) in terms of processability, printing mechanism, and post-treatment. However, as illustrated in Table 2, key differences exist. In DLP, an entire image can be projected using UV light to ensure complete layer curing simultaneously. In contrast, SLA depends on Galvano mirrors to guide only a laser beam that selectively cures specific regions [14]. Consequently, DLP enables faster fabrication compared to SLA. However, the surface finish in DLP depends on the pixel resolution of the projector, whereas SLA typically offers better surface quality due to the precise control of the laser beam [17].

Table 2. Differences between SLA and DLP.

Aspect	SLA (Stereolithography)	DLP (Digital Light Processing)
Resolution	High precision due to the focused laser point	Dependent on the projector pixel density
Fabrication Speed	Slower, due to point-by-point laser curing	Faster, since an entire layer is cured simultaneously via image projection
Energy Consumption	Higher, due to continuous laser operation	Lower, as full layers are cured at once
Materials waste	Comparable: dependent on setup and handling	Comparable: also setup-dependent
Surface Finish	Smoother due to laser precision	Slightly rougher: pixelation possible at layer edges

Table 2. *Cont.*

Aspect	SLA (Stereolithography)	DLP (Digital Light Processing)
Part Size Capability	Suitable for large parts (scalable laser systems)	Limited by projector size and resolution
Post-Processing	Washing and UV post-curing are required	Same as SLA
Applications	Dental models, jewelry, high-detail prototypes	Small/medium parts where speed outweighs detail

DLP typically uses a bottom-up configuration, as shown in Figure 3. In this setup, the projector is located beneath a transparent vat filled with resin, and the build platform is immersed to a depth corresponding to the desired layer thickness. After each layer is cured, the platform moves upward by a defined step, exposing the next layer for curing. This sequence is repeated until the complete object is printed [17].

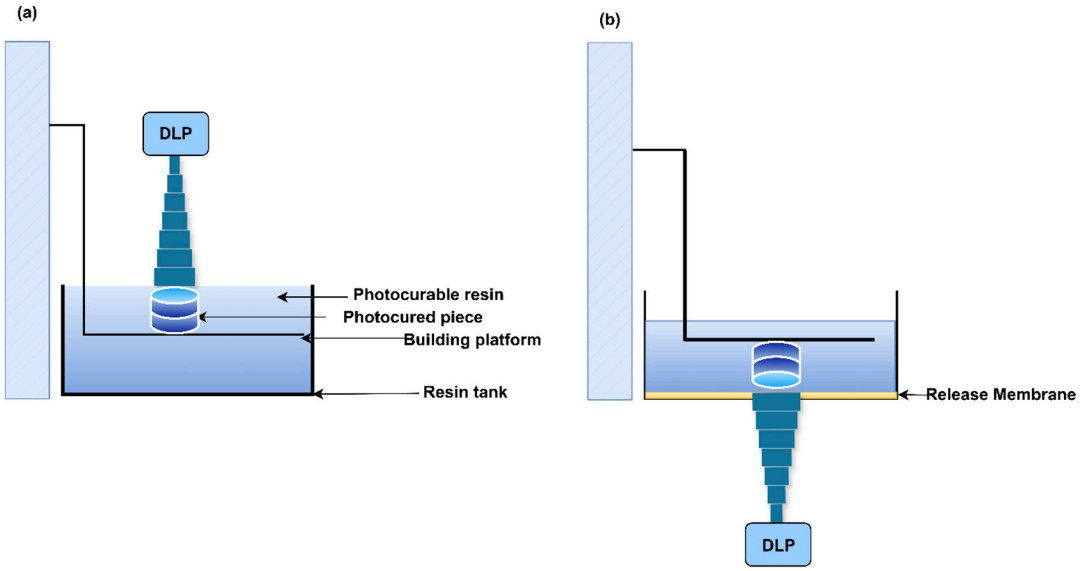


Figure 3. Digital light processing: (**a**) top-down approach and (**b**) bottom-up approach.

In contrast, a top-down configuration positions the projector above the vat. The build platform is submerged slightly below the resin surface, and after curing the first layer, it moves downward layer by layer. The bottom-up setup requires less resin due to its shallower vat, minimizing material waste and costs [17].

Release Membrane

In bottom-up SLA and DLP systems, a release membrane at the base of the vat (also called a container-bed membrane) is essential. This membrane reduces the separation force required to peel cured layers from the vat base when the build platform lifts. The magnitude of this force directly impacts print quality; if it is too high, it can cause printing defects or even part delamination.

Researchers have investigated strategies to reduce the separation force and enhance mechanical integrity.

Pan et al. (2017) [37] studied the use of polydimethylsiloxane (PDMS) membranes at the vat base. They found that thicker membranes enhanced flexibility and absorbed part of the separation force. Furthermore, PDMS's oxygen permeability induced partial layer

inhibition, allowing easier detachment. However, this also resulted in under-cured, brittle samples that required post-curing to achieve full mechanical performance.

Jiang et al. (2022) [38] introduced a porous building platform with a swing mechanism. The permeable surface improved the adhesion of the first layers, stabilizing the print. However, this also increased the separation force from 195.2 N (on the traditional platform) to 220.7 N. The swing mechanism helped counteract this by slightly tilting the vat after each layer, facilitating detachment.

Yang (2022) [39] analyzed parameters influencing separation force, such as exposure duration, slice thickness, platform speed, and tank geometry. They concluded that separation speed (platform lift rate) had the most significant impact; the higher the speed, the greater the separation force.

Moayedi Manizani et al. (2023) [40] confirmed this, noting not only the effect of speed but also the influence of image cross-sectional geometry. Smaller cross-sectional areas led to lower separation forces.

3.1.3. Ceramic-Based Applications of Vat Photopolymerization

Vat photopolymerization has proven highly effective for fabricating ceramics with excellent surface quality and fine detail. These attributes make it especially suited for components in electronics, biomedical devices, and micro-mechanical systems.

Table 3 summarizes key studies and ceramic applications using VAT-based additive manufacturing.

Despite these promising applications, several technical challenges remain. High ceramic loadings are generally desirable for mechanical strength; however, this makes slurry homogenization more difficult. As mentioned before, high solid content greatly increases viscosity, which negatively impacts slurry flowability and layer formation. Additionally, a large refractive-index mismatch between the ceramic particles and the resin increases light scattering, while intrinsic optical absorption can further reduce curing depth.

The key issue lies in UV wavelength penetration. Longer wavelengths may improve penetration when absorption and scattering are reduced, and the photoinitiator remains sufficiently active at the selected wavelength. $BaTiO_3$ shows strong absorption in the typical range of most SLA systems (350–410 nm), reducing light transmission to the resin. This leads to lower cure rates, requiring longer exposures and risking layer delamination, poor interfacial bonding, and mechanical failure.

To address this, Chugunov et al. (2022) [41] adjusted the curing wavelength to 465 nm in $BaTiO_3$-filled slurries, increasing the cure depth from 30 to 50 µm to nearly 100 µm. However, most commercial printers do not support wavelength tuning, making high-index ceramics such as $BaTiO_3$ and lead zirconate titanate (PZT) difficult to process.

An alternative consists of adding polymeric additives to modify the slurry's optical properties. Liu et al. (2024) [42] demonstrated that incorporating 30 vol% polyethylene (PE) into PZT formulations increased the cure depth from <25 µm to ~40 µm (at a fixed 200 mJ/cm^2, 405 nm laser). This was attributed to PE's low UV absorption and improved refractive index matching. However, a higher PE content increases viscosity and reduces ceramic loading, potentially leading to poor densification and structural collapse after debinding.

Similar approaches include modifying the refractive index with additives such as soluble starch (SS) and polystyrene (PS), as shown by Liu et al. (2023) [43] and Liu et al. (2024) [44]. Alternatively, using low-index lead carbonate precursors instead of lead oxide precursors has been shown to improve curing in PZT slurries [45].

Another strategy is tuning the particle size distribution. Liu et al. (2023) [46] showed that blending fine and coarse $BaTiO_3$ particles in a 2:8 ratio improved both processability

and final part strength. Fine particles reduce light scattering, improving curing; however, a dominance of fine grains could increase viscosity, thereby increasing difficulties with slurry processability and printing.

More recently, Cao et al. (2026) [47] investigated curcumin addition to reduce scattering-induced overcuring in DLP ceramic printing. Curcumin absorbs light near the printing wavelength of 405 nm and scavenges free radicals, limiting unwanted polymerization outside the exposed regions. Compared with conventional absorbers such as Sudan I and UV327, it improved printing fidelity over a wider range of exposure doses. In alumina slurries, adding 0.01 wt% curcumin reduced the printed width of a nominal 10 µm line from 66.8 to 26.1 µm in single-layer tests. This result also illustrates the difference between the nominal optical resolution and the actual printed feature size. The approach was extended to ZrO_2, SiO_2, and SiC. For SiC, 0.02 wt% curcumin kept the unresolved fraction of the test pattern below 10% at exposure doses of 80 and 100 mJ/cm^2. However, excessive curcumin concentrations strongly delayed or inhibited polymerization. Its concentration must therefore balance the suppression of unwanted curing with sufficient polymerization in the intended regions.

In summary, advances in slurry formulation, curing strategies, and refractive index optimization are opening new possibilities for processing high-refractive-index ceramics using vat photopolymerization. These innovations are bringing researchers closer to producing exceptionally accurate complex ceramic parts with both superior functional and mechanical properties.

Table 3. Representative applications of photopolymerized ceramic-based materials in AM.

Ceramic	Ceramic Loading	Technique	Debinding (°C)	Sintering (°C)	Density (g/cm^3) or Relative Density (%)	Applications or Potential Ones	Reference
0.71Pb($Mg_{1/3}Nb_{2/3}$) O_3-0.29$PbTiO_3$ (PMN-29PT)	78 wt%	SLA	600	1235 for 2 h	Not reported (NR)	Ultrasonic transducer	[48]
0.99(0.76$Bi_{0.5}Na_{0.5}TiO_3$-0.24$SrTiO_3$)-0.01$NaNbO_3$	40%	SLA	425 for 4 h with a heating rate of 0.2 °C/min.	1120 to 1180.	~5.55 g/cm^3	Bending actuator	[49]
Al_2O_3	40 vol%	SLA	600 with heating rate of 0.2 °C/min	1600 for 2 h	NR	NR	[50]
PZT	NR	DLP	500	1250 for 2 h.	83.12	Hydroacoustic transducers	[42]
Al_2O_3	82 wt%	SLA	1000	1700	99.8	/	[35]
PZT	32 vol%	DLP	395	1250 for 2 h	89.51	Electronic devices, including piezoelectric actuators	[43]
$Pb_{1-x}La_x(Zr_{0.52}Ti_{0.48})O_3$ (PLZT)	NR	DLP	377	1250 for 2 h	NR	Piezoelectric energy harvesting	[45]
$BaTiO_3$	80 wt%.	DLP	600	1350	95.39 ± 0.63	Piezoelectric sensor	[46]
PZT	NR	DLP	NR	1250 for 2 h.	91.43	Electrical applications	[44]
BCZT	~40 vol%	SLA	425 at 0.2 °C/min for 4h	1420 for 3 h	NR	Piezoelectric sensors	[51]

Table 3. *Cont.*

Ceramic	Ceramic Loading	Technique	Debinding (°C)	Sintering (°C)	Density (g/cm^3) or Relative Density (%)	Applications or Potential Ones	Reference
$BaTiO_3$	40 vol%.	DLP	460	1250 1275 1300 1325 for 3 h	NR	Piezoelectric sensors for energy harvesting	[52]
$Sm_{0.025}Pb_{0.9625}$-[$(Mg_{1/3}Nb_{2/3})$ $0.71Ti_{0.29}]O_3$ (Sm-PMN-PT)	40 vol%	DLP	600	1220 for 2 h	98	3–3 piezocomposites for electrical applications	[53]
BCZT	45 vol%. 50 vol% and 55 vol%	DLP	460	1450 for 3 h	NR	Porous piezoceramics for sensors. Energy harvesting and medical applications	[54]
BCZT	10 to 50 vol%.	SLA	425	1380 1400 1420 1440 for 3 h	94.46 at 1420 98.02 for the lamellar structure	Sensing and energy harvesting applications	[55]
PZT	72 wt%	SLA	/	/	/	0–3 composites used as pressure sensors	[56]
SiO_2-Al_2O_3-ZrO_2	NR	DLP	NR	1150 1200 1250 1300	NR	Extreme high-temperature applications	[57]
Al_2O_3	80 wt%	DLP	560	1600 1650	97.4	Industrial applications	[58]
BCZT	40 vol%	DLP	600	1400	96.58	Energy harvesting	[59]
PMN–PZT	48–50 wt%	DLP	/	/	/	Composites for self-powered electronics and sensors	[60]

3.2. Material Extrusion Techniques

This section reviews extrusion-based additive manufacturing methods: fused deposition modeling (FDM) and direct ink writing (DIW). The FDM process and its critical parameters are discussed in depth, along with key challenges and proposed solutions from the literature. The advantages and drawbacks of this technique are summarized. Special attention is given to ceramic-loaded filaments, which are evaluated for printability and process optimization. Ceramic-based applications are also reviewed with respect to fabrication, post-treatment, and current research trends, and key knowledge gaps are highlighted.

Subsequently, the DIW technique is analyzed. Emphasis is placed on the rheological behavior of ceramic-loaded inks, with a detailed discussion of the parameters that influence their printability. Representative applications and post-processing strategies are also addressed.

3.2.1. Fused Deposition Modeling

Fused deposition modeling (FDM), also known as fused filament fabrication (FFF), is one of the most widely used extrusion-based additive manufacturing processes. As illustrated in Figure 4, the process involves feeding a thermoplastic filament, which can be

loaded with functional materials such as ceramics, metals, wood, or glass, through a heated nozzle. The nozzle moves along the X-, Y-, and Z-axes, depositing semi-molten material layer by layer. This process continues until the final 3D object is completed [16].

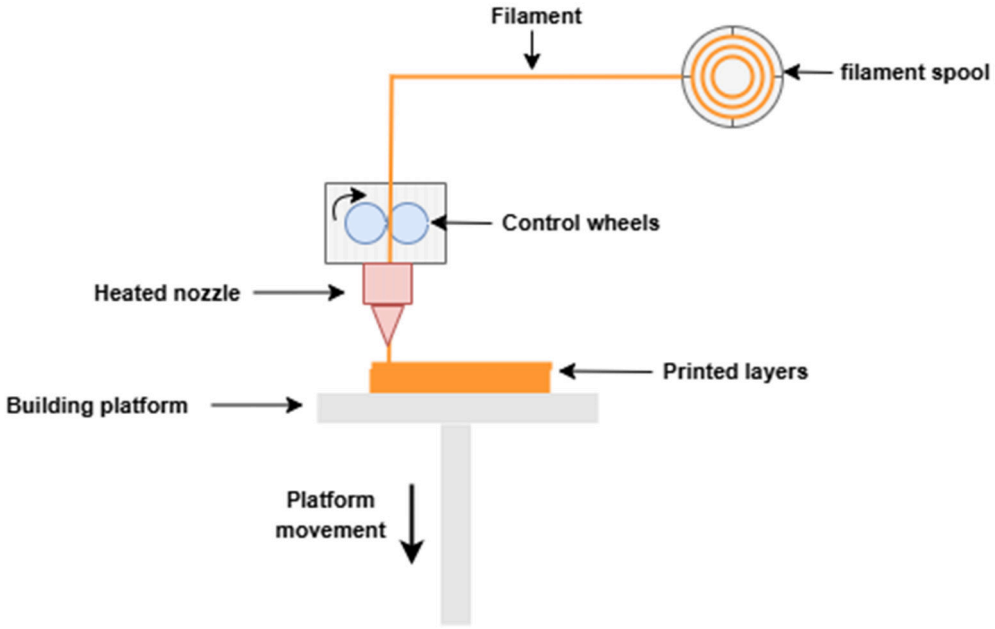


Figure 4. Fused deposition modeling principle.

Process Parameters, Limitations and Advantages of FDM

FDM involves several critical process parameters that govern the final properties of printed components, as shown in Figure 5. These include nozzle diameter, printing speed, layer height, infill percentage, printing temperature, and build orientation. Each of these factors directly influences surface quality, mechanical strength, porosity, and print fidelity.

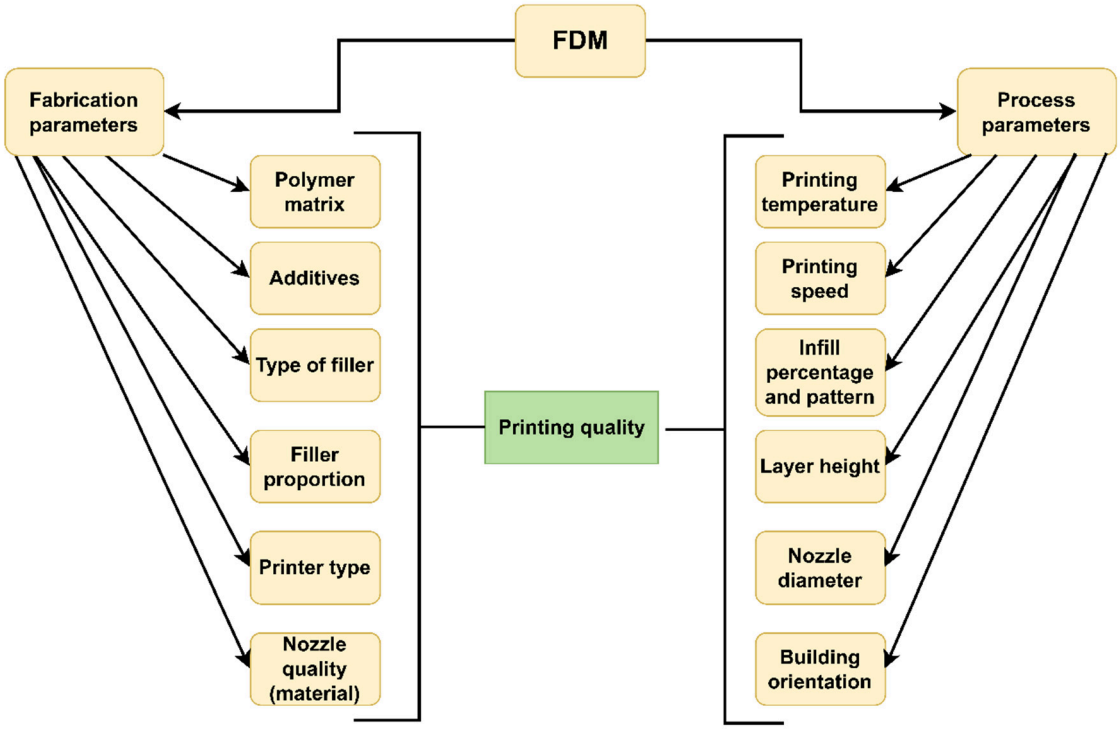


Figure 5. Key parameters governing printing quality in FDM.

Auffray et al. (2022) [61] studied the effects of seven key parameters, namely the infill pattern, layer height, infill density, print speed, raster orientation, outline overlap, and extruder temperature, on Young's modulus and yield strength. They found that the infill density, pattern, speed, and orientation were the most influential, with denser infill enhancing mechanical strength. However, increased infill also leads to greater material usage, longer print times, a slower debinding process, and higher production costs [62].

These process parameters must be adapted to the specific material used to tackle the well-known limitations of the fused deposition modeling technique, such as porosity, which directly affects the mechanical and functional properties. Furthermore, resolution limitations influence the surface finish, thereby affecting the final part details.

Porosity remains a common issue in FDM, arising from voids between deposited layers. This limitation can be mitigated by increasing the nozzle temperature to improve the flow [63] or by optimizing the toolpath to enhance interlayer bonding [64,65]. Additionally, using slightly larger filament diameters (>1.75 mm) has been shown to improve filling by promoting excess deposition [66].

Orlovská et al. (2020) [67] found that using smaller layer heights (0.1 mm) significantly improved flexural strength, modulus, and surface finish in alumina/polylactic acid (PLA) composites with 50 vol% ceramic content. Similarly, Khunt et al. (2022) [63] observed that higher printing temperatures and slower speeds improved interlayer adhesion and density in polyetheretherketone (PEEK)-based prints.

Smirnov et al. (2023) [68] studied different nozzle diameters, layer heights, and infill patterns in 60 vol% Al_2O_3/PLA composites. They concluded that a 0.6 mm nozzle, 0.4 mm layer height, and line infill pattern yielded the best mechanical performance. The line pattern enabled improved contact between layers, reducing voids and enhancing strength.

Similarly, Aw et al. (2018) [69] showed that line infill patterns improved mechanical and thermoelectric performance in acrylonitrile butadiene styrene/zinc oxide (CABS/ZnO) composites.

Build orientation also plays a significant role. Cano et al. (2020) [70] demonstrated that a 0° orientation in zirconia-based prints minimized porosity and maximized bending strength due to better alignment of material with applied stress. This research contributed to understanding the parameters that can reduce porosity and enhance the mechanical properties of the obtained pieces. However, the mentioned parameters are of secondary importance, as the printed pieces must undergo rigorous, indispensable post-processing steps, including multistep debinding and sintering, to obtain fully dense ceramics.

These far more important procedures must be carefully controlled, particularly in components with high infill percentages, to prevent cracking, blistering, or structural collapse. Rapid debinding can cause gas buildup in the interior of dense parts, leading to internal pressure, bubble formation, and degradation of both mechanical and surface properties. Consequently, a slow, controlled thermal debinding step is often preceded by chemical debinding to remove a portion of the binder and create open porosity for gas escape. While effective, this two-step process increases processing time, energy consumption, and cost.

Recent innovations, such as ultrafast high-temperature sintering (UHS), offer promising alternatives. As demonstrated by Bhandari et al. (2024) [71], UHS combines thermal debinding and sintering into a single step, drastically reducing processing time. Their study demonstrated that integrating chemical debinding in acetone for 1 h, coupled with only 30 to 120 s of thermal debinding and sintering, was sufficient to produce fully densified, crack-free components with submicrometric grain sizes comparable to those obtained through conventional methods. This process reduced fabrication time by over 99%, offering a transformative approach to overcoming FDM's limitations in ceramics fabrication.

The resolution and surface finish limitations can also be mitigated by post-processing steps such as electroplating [72], polishing [73], blasting [74], or coating [75]. These treatments reduce surface imperfections and visible layer lines, thereby meeting stringent functional and esthetic requirements.

On the other hand, fused deposition modeling (FDM) offers several notable advantages over other additive manufacturing (AM) techniques, as shown in Table 4. One of its primary benefits is the low cost of both feedstock materials and equipment. The widespread availability of affordable desktop printers significantly reduces the entry cost of fabrication, while the relatively low energy requirements, especially compared to energy-intensive methods such as stereolithography (SLA), further enhance its cost-effectiveness. Additionally, FDM allows for high-speed fabrication, making it particularly well-suited for rapid prototyping.

Table 4. Advantages and limitations of fused deposition modeling (FDM).

Advantages	Limitations
Equipment Cost: Low-cost equipment, widely available and easy to operate.	**Resolution**: Limited resolution compared to other techniques (e.g., SLA, DLP, or PBF).
Material versatility: Compatible with a wide range of thermoplastics and composites, including ceramic-filled polymers.	**Surface Finish**: Poorer surface finish and visible layer lines compared to other AM methods.
Simplicity: Easy to operate with its user-friendly design, with minimal training required.	**Mechanical Properties**: Lower mechanical strength due to layer-by-layer bonding and potential porosity.

Another key strength of FDM lies in its versatility. The technique supports a broad range of materials, including pure thermoplastics as well as composite filaments. This material compatibility has enabled FDM to find applications in diverse fields such as biomedical devices, electronics, and energy harvesting.

Just as technical limitations and post-processing steps are crucial in FDM, filament properties and rheological behavior are equally critical, directly governing printing success. The following sections discuss the challenges encountered in ceramic-loaded thermoplastic filaments and their fabrication process, along with proposed solutions.

Challenges in Ceramics-Loaded Thermoplastic Filaments

As mentioned previously, one of the significant advantages of FDM is its capacity to incorporate ceramics into thermoplastic filaments. Ceramic-filled filaments can follow two distinct routes: direct fabrication of polymer–ceramic composites, in which the polymer remains in the final component, and indirect fabrication of fully ceramic parts, in which the organic phase is removed before sintering. Functional composites are particularly promising for biomedical applications such as bone and tissue scaffolds.

For instance, Mystiridou et al. (2021) [76] reported that scaffolds composed of polycaprolactone (PCL)/PLA loaded with 10 wt% hydroxyapatite (HA) and 5 wt% $BaTiO_3$ improved cell proliferation by 25%, demonstrating strong potential in regenerative medicine. Similarly, Sikder et al. (2022) [77] used $BaTiO_3$/PCL composites to enhance osteogenic performance. Moreover, Zhang et al. (2021) [78] produced poly(L-lactic acid) (PLLA)/nano-hydroxyapatite (nHA) scaffolds with up to 50 wt% nano-hydroxyapatite, achieving high compressive strength and excellent bioactivity.

Aside from biomedical sector compatibility, the energy domain is also an important explored sector in FDM. Sebastian et al. (2021) [79] fabricated 3-3 PZT/epoxy scaffolds via FDM for ultrasonic transducers, reporting a figure of merit of 50 fm^2/N at 25 vol% PZT.

Similarly, Bach et al. (2018) [80] reported further enhancement of piezoelectric properties, achieving a d_{33} of 250 pm/V at 70 vol% PZT. Moreover, the incorporation of $BaTiO_3$ ceramics can improve the dielectric properties of thermoplastics, enhancing permittivity for use in capacitors, sensors, and energy storage devices [81–84].

Despite this advantage, ceramic-loaded filaments present processing challenges. High ceramic loadings increase melt viscosity, which can lead to nozzle clogging. Simultaneously, reduced binder content causes brittleness, resulting in filament breakage and print failure. Particle agglomeration and inconsistent filament diameters further complicate the printing step. Addressing these problems requires optimization in material formulation.

Higher viscosity, primarily due to particle–particle interactions in ceramic-loaded systems, is a major limitation for FDM. Surfactants are commonly added to reduce interparticle friction and enhance dispersion. These amphiphilic molecules interact with both the polymer matrix and ceramic particles, improving compatibility and homogeneity and reducing overall viscosity, as shown in Figure 6.

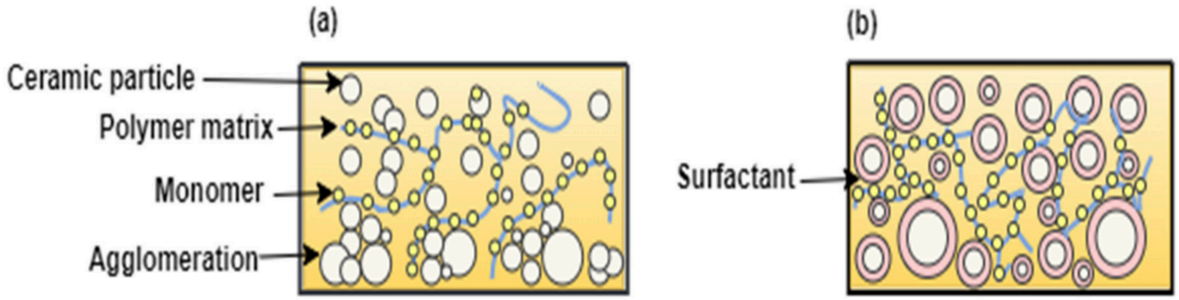


Figure 6. Surfactant effect on composite ceramic/polymer: (**a**) before adding surfactant; (**b**) after adding surfactant.

Stearic acid (SA) is among the most frequently used surfactants [12,65,66,80,83,85,86]. Its hydrophilic head binds to ceramic surfaces while the hydrophobic tail interacts with the polymer, aiding deagglomeration during mixing. However, the surfactant quantity must be optimized. If the specific surface area of the ceramic is significant and insufficient surfactant is added, the viscosity may increase instead [66].

Nötzel et al. (2021) [66] recommended a stearic acid content of 2.2–3.3 mg/m^2 for zirconia filaments. Similarly, Nötzel & Hanemann (2020) [85] used 3.3 mg/m^2 for alumina, achieving homogeneous feedstocks. Excessive surfactant, however, may destabilize the green body and reduce final part strength [66,87].

On the other hand, plasticizers are another strategy explored by researchers [82,88] to reduce brittleness and improve filament flexibility. Unlike surfactants, plasticizers soften the polymer matrix by intercalating between polymer chains, lowering the glass transition temperature (Tg) and melt viscosity. Nevertheless, an excessive softening of the polymer can reduce the mechanical strength of the filaments.

For example, Choi et al. (2018) [89] used polyethylene glycol (PEG) (molecular weight (Mw) = 200) as a plasticizer in PLA–ceramic composites and found improved mixing and reduced Tg. While low-molecular-weight plasticizers provide better flexibility, they may migrate over time, compromising long-term stability. High-molecular-weight alternatives offer greater durability but may affect processing and mechanical strength [90].

Beyond additives, filament fabrication parameters (e.g., mixing and extrusion), equipment parameters (printer type, nozzle diameter, and nozzle material), and even storage conditions (controlled humidity) play critical roles in achieving successful printing outcomes. Optimizing the fabrication process is crucial for producing ready-to-print filaments.

Filament Fabrication Parameters

Several methods are used to fabricate ceramic-loaded filaments. One of the most widely adopted approaches is solvent casting, which involves dissolving the polymer in a solvent and then introducing ceramic powder while maintaining continuous mechanical stirring. After complete dispersion, the solvent is evaporated, yielding a ceramic/polymer mixture that is subsequently pelletized, cut, or ground into feedstock suitable for extrusion. This method is popular due to its simplicity and minimal equipment requirements [76,77,81,82,84,91]. However, it often suffers from suboptimal ceramic dispersion, necessitating prolonged stirring times. Improved homogeneity can be achieved through dual extrusion [77,92], where an initial extrusion is followed by pelletization and a second extrusion step. While this approach enhances dispersion, it can degrade the polymer matrix due to repeated thermal cycling.

Another widely used method involves mixer–kneader or compounder systems, which apply high shear forces to improve mixing quality [12,65,66,80,83,85,86]. Despite their effectiveness, these methods require specialized, often costly equipment.

Alternatively, some researchers have employed ball or planetary milling to enhance dispersion and prevent agglomeration. This is typically followed by casting, sieving, pelletization, and extrusion [93–95]. Notably, a high ceramic loading up to 60 vol% has been achieved using this method, even in the absence of surfactants or plasticizers. Even if the maximum solid loading content depends mainly on the ceramic type and organic matrix, a ceramic loading between 35 vol% and 40 vol% is recommended. This range ensures the integrity of the parts during debinding and sintering, while also facilitating filament handling and the printing process.

In addition to standard printing parameters (e.g., temperature and speed), printer type and nozzle configuration can significantly influence the printability and resolution of ceramic-loaded filaments.

Desktop printers have been widely used [65,67,82,84,85], offering key advantages for short and brittle filaments. Since these setups do not require long filaments to feed through rollers, printing moderately rigid and highly loaded filaments becomes feasible by manually cutting them into ~50 cm lengths [65,66,85].

Nozzle diameter and configuration are equally critical. Larger nozzles reduce the risk of clogging when printing high-viscosity filaments, but at the expense of resolution. Some researchers have modified printer heads to accommodate filaments up to 3 mm in diameter [65] and integrated Titan extruders with gear ratios of 3:1 to ensure consistent feedstock delivery.

Trends and Ceramic-Based Applications of Fused Deposition Modeling

Based on the current literature on ceramic-based filament printing research, the process parameters, post-treatment conditions, and applications are summarized in Table 5. Ceramic loadings up to 50 vol% are technically achievable. However, printable limits depend on both the ceramic properties and the compatibility of the binder system. A 30 vol% ceramic content is commonly printable and sufficient for ceramic/polymer composites. For fully densified ceramics, however, this loading is typically inadequate because binder removal during debinding creates large voids that can cause structural collapse.

When the ceramic content exceeds 35 vol%, filaments become increasingly brittle and prone to breakage. At >45 vol%, stick–slip behavior often occurs, a phenomenon where filament motion alternates between sticking and slipping due to elevated nozzle friction [83]. This leads to irregular material flow, poor interlayer bonding, and surface defects. To address this, researchers suggest using larger nozzle diameters, reducing printing speeds, or applying Teflon coatings to minimize nozzle-filament friction [83].

Table 5. Representative studies on the fabrication of ceramic-loaded filaments and their processing conditions.

Feedstock	Max Ceramic Percentage	Polymer Matrix	Additives	Nozzle Size (mm)	Debinding (°C)	Sintering (°C)	Density (%)	Applications or Potential Ones	Reference
PZT $BaTiO_3$	49 vol% 52 vol%	Ethylene–vinyl acetate (EVA)	SA (surfactant)	0.8	Up to 500	1200 1350	NR	3-3 composites for hydrophone in underwater noise detection	[80]
HAp and/or $BaTiO_3$	20 phr Hap/ 20 phr $BaTiO_3$	PCL/PLA	NR	0.4	/	/	/	Composites for bone regeneration	[76]
$BaTiO_3$	45 vol%	PCL	NR	0.4	/	/	/	Composites for bone regeneration	[77]
$BaTiO_3$	9 wt%	Polyvinylidene fluoride (PVDF)	NR	NR	/	/	/	Nanocomposite-based materials for sensors. actuators. and dielectric devices	[81]
$BaTiO_3$	32 vol%	Acrylonitrile–butadiene –styrene (ABS)	1 wt% octyl galate (surfactant) + 5 wt% dibutyl phthalates (plasticizer)	NR	/	/	/	Optical devices	[82]
Al_2O_3	60 vol%	PLA	NR	0.4 0.6 0.8	Up to 600	1550 (2 h)	91	NR	[94]
$BaTiO_3$	35 vol%	ABS	SA (surfactant)	0.3	/	/	/	Capacitors. Lightweight passive antennas	[83]
Al_20_3	50 vol%	LDPE (low density polyethylene + Paraffin	SA (surfactant)	0.15 0.3 0.4	Chemical debinding in n-hexane and thermal debinding up to 500	1400 for 6 h	98.4 for open structures 97.3 disks	Prototypes and design studies	[65]
$BaTiO_3$	29 vol%	ABS	NR	Two-nozzle printer	/	/	/	Electromagnetic devices	[84]
Al_2O_3	50 vol%	PEG/polyvinyl butyral (PVB)	SA (surfactant)	0.25	Chemical debinding in water. Thermal debinding up to 500	1400 for 6 h	98	NR	[85]
$BaSrTiO_3$	15.26 vol%	ABS	NR	0.55	/	/	/	Prototype microstrip patch 5G antenna and a hemispherical dielectric lens	[91]
Al_2O_3	60 vol%	PLA	NR	0.6	/	/	/	NR	[93]

Table 5. *Cont.*

Feedstock	Max Ceramic Percentage	Polymer Matrix	Additives	Nozzle Size (mm)	Debinding (°C)	Sintering (°C)	Density (%)	Applications or Potential Ones	Reference
ZrO_2	50 vol%	LDPE + paraffin wax (PW)	SA (surfactant)	0.4	Chemical debinding in n-Hexane. Thermal debinding up to 500	1450 for 3 h	99	NR	[66]
Barium ferrite ($BaFe_{12}O_{19}$)	35 vol%	ABS	SA (surfactant)	0.4	/	/	/	Magnetic composites	[86]
Al_2O_3	50 vol%	PLA	NR	0.8	/	/	/	NR	[95]
ZrO_2 stabilized with 3 mol% yttria (Y_2O_3)	47 vol%	Acrylic acid-grafted high-density polyethylene AA-(HDPE) + styrene–ethylene–butylene–styrene (SEBS)/(PW)	SA (surfactant)	0.6	Chemical debinding in cyclohexane. Thermal debinding up to 600	Pre-sintering up to 1050	NR	NR	[12]
Mullite ceramic	50 vol%	Thermoplastic polymer	AAK (aliphatic fatty acid) as surface adhesion modifier, glycol-based softener (plasticizer)	0.4 0.6	Up to 850	1200 1300 1400	NR	NR	[88]
Al_2O_3	50 vol%	NR	NR	0.4	Chemical debinding in cyclohexane. Thermal debinding up to 850	1600 for 1 h	80–89	NR	[67]
ZrO_2 stabilized with 3 mol% yttria (Y_2O_3)	47 vol%	Thermoplastic elastomer compound (TPE) Polyolefin grafted with a polar component	NR	0.6	Chemical debinding in cyclohexane. Thermal debinding up to 440	1365 for 3 h	>98	NR	[70]
Al_2O_3	60 vol%	PLA	NR	0.6 0.8 1	Up to 600	Up to 1550 for 2 h	93	NR	[68]
Al_2O_3	50 vol%	EVA	SA (surfactant)	0.6	Up to 500	Pre sintering 1000 Sintering up to 1600 for 1 h	NR	NR	[87]

Table 5. *Cont.*

Feedstock	Max Ceramic Percentage	Polymer Matrix	Additives	Nozzle Size (mm)	Debinding (°C)	Sintering (°C)	Density (%)	Applications or Potential Ones	Reference
Al_20_3	80 wt%	Industrial binder kcmix 33	Dolapix CE 64 (surfactant)	0.6	Chemical debinding in acetone. Thermal debinding up to 800	1550 for 2 h	~92	NR	[96]
$BaTiO_3$	45.8 vol%	Polyvinyl alcohol (PVA)/PCL	NR	0.3 0.4	Chemical debinding in toluene. Thermal debinding up to 1000	1200 1250 1300 1350	~92	NR	[92]
Al_2O_3	53 vol%	EVA/PW/HDPE	NR	0.6	Thermal debinding up to 550	1350 1500 1600	NR	NR	[97]

Ultimately, an in-depth rheological analysis remains crucial for achieving a stable formulation and ensuring successful printing.

Moreover, FDM is rapidly evolving, with recent efforts focused on improving efficiency, expanding material compatibility, and addressing sustainability concerns.

Among the most impactful developments is the integration of multi-nozzle printing systems. These systems allow simultaneous deposition of multiple materials, enabling graded or multifunctional structures. For example, Castles et al. (2016) [84] used a dual-nozzle printer to fabricate structures combining pure acrylonitrile–butadiene–styrene (ABS) with 50 wt% $BaTiO_3$-loaded ABS, enabling the fabrication of photonic components such as omnidirectional reflectors and waveguides. While this approach enhances design flexibility, it also introduces challenges related to interfacial adhesion and thermal expansion mismatch, which require careful control during processing.

Environmental sustainability has emerged as a major focus area. Bio-sourced and biodegradable polymers such as PLA (polylactic acid) and PCL (polycaprolactone) are increasingly being adopted as matrix materials to reduce environmental impact. However, their mechanical performance, thermal stability, and long-term durability often fall short of those of conventional polymers, limiting their use in high-performance applications.

Another promising trend is the integration of shape memory polymers (SMPs), which exhibit reversible deformation in response to external stimuli. This has facilitated the emergence of 4D printing, wherein the printed object undergoes a functional transformation over time. Applications include adaptive textiles for extreme environments and self-adjusting prosthetics [98]. While conceptually transformative, current SMP-based systems face limitations related to recovery time, fatigue resistance, and large-scale manufacturability.

Despite these advances, several technical barriers persist. A primary challenge in ceramic FDM is achieving high ceramic loadings (>45 vol%) without compromising filament printability. At high loadings, poor dispersion and weak interactions between the ceramic particles and polymer matrix increase brittleness, leading to filament breakage and print failure. Additionally, a high ceramic content often leads to stick–slip behavior during extrusion as a result of elevated interfacial friction between the filament and nozzle. This phenomenon causes inconsistent material flow, dimensional inaccuracies, and weak interlayer adhesion. Larger nozzle diameters, reduced printing speeds, and Teflon-coated nozzles have been proposed to mitigate these issues [83], but a more fundamental understanding of material rheology remains essential.

Sinterability is also a limiting factor. While 30 vol% or less ceramic loading is generally sufficient for producing ceramic/polymer composites, it is inadequate for achieving fully densified ceramic parts after debinding. Loadings of at least 35–40 vol% are often necessary to avoid structure collapse, which further increases the impact on the filament flexibility and extrusion behavior. Innovative binder systems and optimized particle packing strategies are needed to tackle these limitations.

Moreover, the debinding and sintering steps continue to be bottlenecks in terms of time and energy consumption. Rapid sintering techniques such as UHS and microwave sintering have demonstrated potential to streamline these steps, but further investigation is needed to validate long-term mechanical and functional performance.

Another critical research gap concerns the rheological modeling of highly filled filaments. Comprehensive studies on material flow under dynamic conditions are necessary to develop robust predictive tools. Machine learning (ML) and artificial intelligence (AI)-driven methods could accelerate this process by enabling data-driven optimization of formulation and process parameters.

Furthermore, while materials such as Al_2O_3, ZrO_2, and $BaTiO_3$ dominate current research, doped ceramics represent a largely unexplored yet highly promising frontier. For example, $BaTiO_3$ co-doped with (Li^+-La^{3+}) [99], (Sn, Ca) [100–102], or the insertion of Li/Ca/Co/Nb [103] has shown improved piezoelectric coefficient d_{33}, electromechanical coupling factor kp, and sinterability. Certain dopants, such as Li [104] and LiF [105], can even reduce sintering temperature, making them ideal candidates for energy harvesting and sensing devices fabricated via FDM.

Finally, there remains a significant gap in translating material and process innovations into fully functional devices. While progress has been made in filament development and feasibility demonstrations, few studies have advanced to prototype-level systems in real-world conditions. Bridging this gap, particularly in application areas such as aerospace, healthcare, and flexible electronics, will be key to elevating FDM into a mainstream technology for advanced manufacturing.

3.2.2. Direct Ink Writing (DIW)

FDM is not the only technique that relies on the extrusion principle. Direct ink writing (DIW) uses a similar extrusion process, as illustrated in Figure 7. Instead of melting thermoplastic filaments, this method extrudes pastes, gels, or slurries at room temperature using different dispensing mechanisms, either pneumatically, mechanically with a plunger, or via a screw device, making it an energy-efficient additive manufacturing technique. This method is especially well-suited for ceramic-loaded pastes.

Process Parameters

DIW operates on principles similar to fused deposition modeling (FDM), making printing parameters such as nozzle diameter, printing speed, layer height, and raster pattern equally important. However, some parameters differ, particularly environmental conditions such as temperature and humidity, as well as immersion in air/oil baths. Still, the single most influential factor in determining the printing quality of DIW parts is the rheology of the ink or paste.

Achieving successful printing and high-quality ceramic structures in DIW requires precise control over rheological properties. Several factors, including the binder composition, filler type and proportion, and particle characteristics such as density, morphology, and size, influence rheological behavior.

Suspension Stability Mechanisms

To maintain the stability of highly loaded suspensions, three primary stabilization mechanisms are employed: electrostatic, steric, and electrosteric stabilization [106]. These mechanisms are summarized in Table 6, along with their respective advantages and limitations.

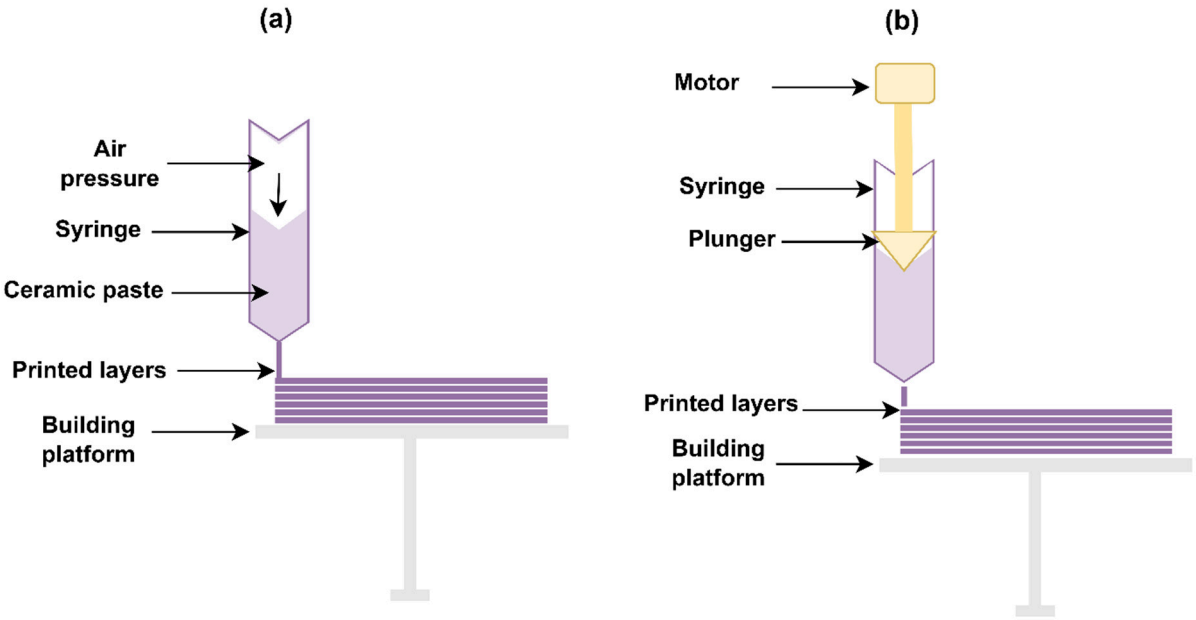


Figure 7. Direct ink writing principle: (**a**) air-propelled paste; (**b**) plunger-propelled paste.

Table 6. Mechanisms of suspension stabilization in DIW-based additive manufacturing.

Stabilization Type	Mechanism	Advantages	Limitations
Electrostatic	Charge repulsion via zeta potential	Effective in low-viscosity, dilute suspensions	Weakened by high solid loading and ionic strength
Steric	Polymer chains create a repulsive barrier	Works in both aqueous and non-aqueous systems	Requires precise polymer concentration to avoid depletion flocculation
Electrosteric	A combination of charge repulsion and steric hindrance	Ideal for high solid-load pastes (>40 vol%)	Requires optimization of pH and dispersant ratio

Electrostatic stabilization relies on charge repulsion between particles, governed by the zeta potential. A high absolute zeta potential ($\zeta > 30$ mV) indicates strong repulsive forces, effectively preventing particle aggregation. However, this mechanism works best in low-viscosity, dilute suspensions. In highly concentrated or high-ionic-strength systems, the electric double layer is compressed, reducing its repulsive effect.

Steric stabilization involves the adsorption of polymeric dispersants onto the ceramic surface, creating a steric barrier that inhibits particle contact and aggregation. This method is suitable for both aqueous and non-aqueous systems and is particularly effective in high-viscosity formulations. However, the polymer concentration must be carefully controlled—excess polymer may lead to depletion flocculation, ultimately destabilizing the suspension.

Electrosteric stabilization combines electrostatic and steric mechanisms, offering superior stability for concentrated suspensions (>40 vol%). This approach overcomes the individual limitations of each method and maintains repulsion forces even at high particle loadings. However, it requires precise control over both pH and polymer content, making formulation optimization more complex.

Composition and Rheological Behavior of DIW Inks

A typical DIW ink consists of three essential components: dispersants, binders (or thickeners), and coagulants. Dispersants (e.g., polyelectrolytes, polymeric surfactants) reduce van der Waals attractions between particles to ensure uniform dispersion and prevent agglomeration. Binders increase the viscosity and promote shear-thinning behavior, giving the ink structural integrity. Coagulants are added to trigger solidification upon extrusion, which prevents slumping and improves the dimensional stability of the printed object.

For optimal printability, the ink must exhibit shear-thinning behavior, where viscosity decreases under shear stress during extrusion and recovers once the material is deposited. This behavior prevents nozzle clogging while ensuring shape retention post-deposition.

The viscoelastic properties of the ink are defined by the storage modulus (G′) and the loss modulus (G″). G′ represents elastic behavior, crucial for maintaining shape after printing, while G″ reflects viscous behavior, which governs flow during extrusion. A sufficiently high G′ is necessary to prevent layer collapse, although excessively high values may impair interlayer adhesion and surface quality. Likewise, an adequately high G″ ensures smooth extrusion, but if too high, it can hinder flow control and lead to erratic extrusion. Therefore, a balance between G′ and G″ is essential. G′ must dominate post-extrusion for shape fidelity, while G″ must be high enough for continuous, controlled flow [107].

Another critical parameter is yield stress, which marks the transition between solid and liquid behavior. In oscillatory amplitude sweeps, the crossover between G′ and G″ is sometimes used as an operational indicator of yielding, although the determined value depends on the selected rheological protocol; a yield stress exceeding 200 Pa is generally required to ensure that printed structures can support their own weight [108]. This value dictates whether the ink can be smoothly extruded and rapidly solidify into a stable form [109].

Yield stress is influenced by solid loading, as well as the properties of the ceramic and organic components. Gadea et al. (2021) [110] found that at 35–40 vol% ceramic content, both yield stress and viscosity increase sharply, shifting rheology from Newtonian or quasi-Newtonian to shear-thinning. In PZT-based inks, this transition occurs at around 52 vol% [111]. Additives such as dispersants, solvents, and plasticizers can modify these thresholds, making comprehensive rheological evaluation essential when tuning formulations.

Insufficient yield stress can lead to slumping during printing [110]; moreover, the maximum printable height is also linked to the yield stress; a higher yield stress allows for taller prints without deformation or structure collapse under gravitational forces, following Equation (2).

$$H_{max} = \frac{\sigma^{Dyn}}{\rho \cdot g} \quad (2)$$

where

σ^{Dy} is the dynamic yield stress (Pa);

ρ is the density (kg·m^{-3}), and g the gravitational acceleration (g = 9.81 m·s^{-2}).

Finally, the choice of extrusion environment can impact part quality. Extruding in oil may cause void formation [112], while air extrusion may result in premature drying and crack development. Alternative strategies, such as cold isostatic pressing (CIP) post-printing, may help mitigate these issues [112].

Impact of Filler Properties on Rheology

The type and content of ceramic fillers play a critical role in determining the rheological behavior and printability of DIW inks. Increasing the filler content enhances viscosity, which poses challenges for extrusion, but simultaneously reduces binder content, thereby minimizing shrinkage during debinding and sintering and preserving dimensional accuracy.

Particle morphology also significantly affects flow behavior and final properties. Spherical particles, due to their reduced friction and lower interparticle interactions, improve

ink flowability and allow for higher solid loadings while maintaining suitable rheological characteristics. In contrast, irregularly shaped particles interlock more effectively, increasing viscosity and reducing flowability; however, they contribute to improved packing density, enabling higher densification during sintering [113].

Thus, while spherical particles support processability, irregular particles offer superior mechanical integrity in the sintered state. Striking an optimal balance between shape, dispersion, and loading is therefore crucial for achieving both printability and enhanced final performance [113].

In this context, Renteria et al. (2021) [114] demonstrated that a bimodal particle size distribution in $BaTiO_3$ powders significantly improved packing density, resulting in enhanced relative density and superior piezoelectric properties.

Ceramic-Based Applications of Direct Ink Writing

Based on the studies summarized in Table 7, direct ink writing (DIW) of ceramic-loaded inks is feasible. Still, it represents a compelling strategy for overcoming geometric constraints found in traditional ceramic shaping methods. DIW is particularly effective for fabricating porous structures and scaffolds, core applications of this technique, and can be coupled with complementary approaches such as cold isostatic pressing (CIP) to achieve higher density and improved mechanical properties [111,112].

Furthermore, DIW benefits from its inherently low organic content. With typical binder levels of 0–5 wt%, the DIW inks allow rapid thermal debinding directly after solvent evaporation. This presents a significant advantage over other AM techniques, such as vat photopolymerization (20–30 wt% binder) and fused deposition modeling (15–20 wt% binder), both of which require time-intensive, multi-step debinding protocols. For instance, Bhandari et al. (2024) [71] demonstrated that FDM-fabricated parts require at least one hour of chemical debinding in acetone, followed by up to 120 s of thermal debinding and sintering. In contrast, parts produced by DIW [115,116] achieve this in a single, accelerated step, making it a more energy-efficient and economically viable alternative.

In conclusion, direct ink writing offers several advantages over other additive manufacturing (AM) techniques, particularly in terms of cost-effectiveness, sustainability, and material compatibility. Unlike vat photopolymerization techniques that require complex light-based systems and custom resin formulations, direct ink writing operates via direct extrusion of ceramic pastes at ambient temperatures. This simplicity significantly reduces equipment costs, energy usage, and material waste, positioning this technique as a highly sustainable and accessible method for ceramic fabrication.

One of DIW's greatest strengths is its ability to process highly loaded ceramic pastes often exceeding 60 vol%, which, after sintering, yield dense components with excellent mechanical, thermal, and electrical performance. Such attributes make DIW particularly suitable for applications such as piezoelectric devices, bioceramic scaffolds, and solid-state energy storage systems. However, achieving high solid loadings requires precise control over the ink formulation and rheology to prevent defects such as agglomeration or nozzle clogging. The incorporation of surfactants or tailored solvent systems is often necessary to maintain stable, homogeneous pastes.

Despite these strengths, DIW has some limitations. Compared to fused deposition modeling (FDM), the range of printable materials is more constrained, primarily because the process is paste-based. Moreover, extensive post-processing, including drying, debinding, and sintering, is essential to achieve the required densification, which increases total production time. Shrinkage control remains critical to ensure dimensional accuracy, and the technique may not yet be suited for large-scale industrial production.

Table 7. Selected studies on ceramic-loaded inks for direct ink writing.

Composition	Ceramic Loading	Solvant	Additives	Printing Parameters	Drying (°C)	Debinding (°C)	Sintering (°C)	Density (%)	Applications or Possible Ones	Reference
$Ba_{0.99}Ti_{0.99}Ca_{0.01}$-$Co_{0.005}$: Nb0.005$O_3$-δ. 1% Li_2CO_3	80 wt%	Terpineol	2.2-butoxyethoxy-ethyl acetate (BEEA) as a dispersant PEG-200 as a plasticizer PVB as a binder	Nozzle of 1 mm Infill speed was 3 mm/s while reducing down to 2 mm/s for the perimeters. Fill density was set at 100%	60 for 3 h	600 for 4 h with a slow increasing rate of 1 °C/min	1100 for 4 h at a rate of 3 °C/min	95	Piezoceramic transducer	[117]
$BaTiO_3$	50 and 52 vol%	Distilled water	Bermocoll E 320 FQ. as binder Darvan 821-A as dispersant Polyethyleneimine (PEI) branched: average Mw = 25,000 as coagulant	Extrusion speed of 5 mm/s and 1.5 mm nozzle size.	NR	600 for 1 h with a heating and cooling rate of 1 k/mn	1350 for 3 h in air with a heating and cooling rate of 5 K/mn	98	Sensing and energy harvesting applications	[112]
$BaTiO_3$	28.5 vol%	Water	(PVA) (Mw ~ 89.000–98.000) was used as a binder Polyacrylic acid (PAA) was used as a lubricant	0.6 mm nozzle size.	Freezer at −5 for 2 h to promote some initial water evaporation by sublimation.+ 40 °C for 24 h	Debinded at 600 for 2 h using a 4 °C/min ramp	1250 for 2 h with a 4 °C/min ramp and cooled down at 4 °C/min to room temperature (RT)	89.97	NR	[114]
$BaTiO_3$	75.1 wt%	Deionized (DI) water	PVA PEG–400 Solsperse 20000 hyper-dispersant	Printing speed was set at 5 mm/s. The layer height was 0.5	NR	500 and 600 for 2 h (1 °C/min)	1300 (1 °C/min)	94	Pressure sensor. Energy harvesting and storage device	[118]

Table 7. *Cont.*

Composition	Ceramic Loading	Solvant	Additives	Printing Parameters	Drying (°C)	Debinding (°C)	Sintering (°C)	Density (%)	Applications or Possible Ones	Reference
$BaTiO_3$	40 vol%	Glycerol and water	NR	Nozzle: 0.410 mm. Extrusion speed was set at 5 mm/s, and infill density was set at 90%	Room temperature for 24 h	10 °C/h up to 300, a 2 h isothermal hold	Heating at a rate of 60 °C/h to 1250–1350, and a 20 h isothermal hold. Finally, cooling to room temperature at a rate of 200 °C/h	96	NR	[110]
$BaTiO_3$	80 wt%	distilled water and glycerol (Prolabo) as solvents	Na-alginate as binder and sodium polyacrylate(Na-PAA) as dispersant	Nozzle of 0.41 mm	Room temperature for 4 h	Single step for debinding and sintering with different thermal treatment technologies (conventional, ultrafast high-temperature sintering (UHS), pressureless spark plasma sintering (PSPS), and fast-firing (FF))	FF preheated furnace (Clasic-0617E) and held at the desired temperature (typically between 1300, 1325, 1350 °C) for 5 min	95	NR	[115]

Table 7. *Cont.*

Composition	Ceramic Loading	Solvant	Additives	Printing Parameters	Drying (°C)	Debinding (°C)	Sintering (°C)	Density (%)	Applications or Possible Ones	Reference
Al_2O_3	42.8 vol% and 48.1 vol% Alumina	Distilled water	Na-polyacrylic acid as dispersant, Na-alginate as binder, and glycerol as humectant	0.41 mm and 0.84 mm The infill density was set to 50%	Drying for 12 h	Single step for debinding and sintering with different thermal treatment technologies. Ultrafast high-temperature sintering (UHS). Pressureless spark plasma sintering (PSPS) and fast-firing (FF).	Different rapid sintering treatments: UHS:301W, 90 s	98	NR	[116]
PZT	52.5 vol%		The dispersant (DISPERBYK-180) glycerol (assay ≥ 99%) and PVA (molecular weight: 31.000–50.000; assay ≥ 99%)	0.4 mm nozzle	80 for 12 h	600 ◦C for 2 h at a slow heating rate of 0.3 °C/min and then cooled at a cooling rate of 5 °C/min	1200 for 2 h at heating and cooling rates of 5 °C/min	97	Sensors or energy harvester devices	[111]
$(K.\,Na)NbO_3$-$(Na_{0.52}K_{0.4425}$-$Li_{0.0375})(Nb_{0.87}$-$Sb_{0.07}Ta_{0.06})O_3$	56 wt%	Mix of methyl methacrylate and pen-taerythritol triacrylate	NR	NR	NR	NR	1100 for 2 h with 3 °C/mn	98	NR	[119]

Table 7. *Cont.*

Composition	Ceramic Loading	Solvant	Additives	Printing Parameters	Drying (°C)	Debinding (°C)	Sintering (°C)	Density (%)	Applications or Possible Ones	Reference
$BaTiO_3$/PDMS	80 wt%	Ethyl acetate	NR	0.8 mm nozzle diameter; 200 mm/min printing speed	NR	NR	NR	NR	NR	[109]
PZT	52 vol%	NR	An aqueous solution containing 10 wt% PVA and PZT powder was prepared. Incorporating 1.75 wt% glycerin as a lubricant and either ammonium polyacrylate (PAA-NH_4) or sodium polyacrylate homopolymer (PAAS) as a dispersant	Printing speed: 8 mm/s; nozzle: 0.6 mm; height of the printing layer was 0.3 mm	NR	700 at a heating rate of 1 °C/min. Holding the temperature at 170, 250, 375, and 600 for 1 h	1250 at a rate of 3 °C/min. Hold for 4 h	97.8	3-3 composites for underwater acoustic transducer	[120]
PLZT$Pb_{0.93}La_{0.07}$-$(Zr_{0.65}Ti_{0.35})_{0.9825}$-$O_3$	70 vol%	Deionized water	1 wt% deflocculant sodium citrate dihydrate	NR	48 h in air	800 for 1 h, with a heating rate of 150 °C/h	1200 for 4 h with a heating rate of 150 °C/h	99.3	3-3 composites for acoustic transducer	[121]

Table 7. *Cont.*

Composition	Ceramic Loading	Solvant	Additives	Printing Parameters	Drying (°C)	Debinding (°C)	Sintering (°C)	Density (%)	Applications or Possible Ones	Reference
PZT	52 vol%	Deionized water	Cellulose solution (Methylcellulose M20) was added as a binder	0.26 mm nozzle. Printing speed was 8 mm/s	NR	1 ◦C/min from 25 °C to 600 °C	5 °C/min 1250 °C. Hold for 2 h	98	Sensing applications	[108]
PZT	80 wt%	Deionized water	(PVA-1788) was used as a binder. Glycerol, triethyl phosphate (TEP), and dibutyl phthalate (DBP) were used as plasticizers	0.4 nozzle	48 h drying	NR	1250 for 2 h	98	3-3 composites that can have Applications in fields of robotics and wearable devices	[122]

4. Critical Comparative Analysis of Vat Photopolymerization and Extrusion-Based Techniques

An overall comparison of the four techniques is presented in Table 8. However, despite their growing adoption in ceramic additive manufacturing, vat photopolymerization (SLA/DLP) and extrusion-based technologies (FDM/DIW) differ fundamentally in terms of processability, material compatibility, and achievable performance. A comparative understanding of these techniques remains limited in the literature, as current studies often focus on specific applications rather than providing comprehensive cross-process comparisons. Therefore, this section critically evaluates these technologies with respect to material requirements, achievable densities, processing constraints, and scalability. Moreover, even if Table 8 offers some direct comparison for some parameters such as shrinkage, due to the existing data for the same material, the other values such as printer speeds, resolutions, and build volume are not universal and are completely dependent on the apparatus used. Moreover, final object properties such as resolution, shrinkage, and relative density depend on several parameters such as ceramic type and loading, slurries, and paste or filament homogeneity, and printing conditions and parameters such as printing speed, heat, and environment.

4.1. Ceramic Powder Characteristics and Feedstock Requirements

Particle size distribution, morphology, specific surface area, and surface chemistry influence ceramic loading, feedstock behavior, and final part properties.

For SLA and DLP, the powder properties must meet rheological and optical requirements. Liu et al. [123] reported that increasing $BaTiO_3$'s particle size reduced suspension viscosity, whereas curing ability decreased significantly when particle size approached the irradiation wavelength. Consequently, improved flow does not necessarily imply improved curing. Particle grading provides another way of adjusting curing depth and final properties. In a DLP study, Liu et al. [46] combined $BaTiO_3$ powders with median diameters of 149 and 879 nm at a ceramic loading of 80 wt%. Increasing the coarse-particle fraction reduced viscosity but also decreased the curing depth. The finer particles were nearly spherical, whereas the coarser particles were irregular. A fine-to-coarse mass ratio of 2:8 achieved a relative density of 95.39% after sintering at 1350 °C. Although SLA and DLP differ in exposure strategy, these studies show that particle size distribution and morphology should be considered together when formulating photopolymerizable slurries, as these parameters influence both printing behavior and final properties. In FDM, the powder characteristics influence the melt flow and must be considered together with the filament feedability. Nötzel et al. [65] used alumina with a median particle diameter of 0.1 µm and a specific surface area of 12 m^2/g. A formulation containing 50 vol% ceramic could be printed through a 150 µm nozzle, whereas increasing the loading to 60 vol% caused feeding difficulties associated with excessive viscosity. Surface properties also affect additive requirements: in zirconia feedstocks, stearic acid additions were evaluated relative to powder surface area, together with adjustments to binder composition [66].

Table 8. Comparative table of additive manufacturing techniques.

Technique	Material Form	Ceramic Solid Loading	XY Resolution	Z Resolution	Printing Speed	Maximum Build Size	Surface Quality	Debinding Difficulties	Sintering Shrinkage	Final Relative Density	Material Compatibility	Cost	Scalability
Stereolithography (SLA)	Ceramic-loaded photocurable slurries	40–61.9 vol% (based on presented research)	Laser spot diameter ≈60 µm (3DCERAM C101 EASY LAB)	20–125 µm (Z-axis movement) (C101 EASY LAB)	Moderate to fast. Due to sequential laser scanning	100 × 100 × 150 mm C101 EASY LAB)	Smooth (fine features possible)	Cleaning, controlled resin burnout. Decomposition gases can cause cracking if the heating cycle is unsuitable	13.5%, for alumina Based on 61.9 vol% ceramic-loaded slurry [124]	94.46–99.8	Less adapted for refractive powders	Expensive. Laser/recoating equipment, formulated resin, cleaning, and furnace processing contribute to cost	The emergence of multi-laser machines can support moderate volume production
Digital light processing (DLP)	Ceramic-loaded photocurable slurries	32–55 vol% (based on presented research)	63 µm lateral resolution (CeraFab S320, Lithoz)	20–200 µm (CeraFab S320)	Whole-layer exposure: up to 150 layers/h on the (CeraFab S320)	257.6 × 135.8 × 320 mm (CeraFab S320)	Smooth (fine features possible)	Cleaning, controlled resin burnout. Decomposition gases can cause cracking if the heating cycle is unsuitable	Approximately 12% for horizontally printed and 17% for vertically printed alumina based on 83 wt% ceramic-loaded slurry [125]	83.12–98%	Less adapted for refractive powders	Expensive. Projection equipment, formulated resin, cleaning, and furnace processing contribute to cost	Projected layer can support batch production
Fused Deposition Modeling (FDM)	Ceramic-loaded thermoplastic filament	45.8–60 vol% (based on presented research)	Hundreds of microns	50–200 µm [126] (Rapide Lite 500)	50-100 mm/s (Rapide Lite 500)	500 × 500 × 500 (Rapide Lite 500)	Moderate (visible layer lines)	Organic elimination by slow heating cycles. Stress- and gas-related defects	x, y = 23.1% ± 1% z = 25.65% ± 1% specified for Zetamix (Nanoe) alumina filaments (45 vol% ceramic loading)	80–99%	All studied ceramics	Moderate. Desktop printers contribute to lowering cost. However, the extrusion process in filament preparation and furnace processing contribute to raising costs	Automated filament feeding and moderate to high printing speeds make it a reliable prototyping machine for moderate to high production capacity
Direct Ink Writing (DIW/Robocasting)	Ceramic paste or ink	28.5–70 vol% (based on presented research)	Hundreds of microns	Hundreds-of-microns [126]	Moderate depending on apparatus	200 × 200 × 200 mm 3D CERAM M.A.T. Basic with DIW option	Moderate (dependent on ink stability)	Drying, binder removal. Organic content controls burnout requirements, while drying adds a separate deformation risk	Between 16% and 18% for a 49 vol% loaded alumina paste [127]	90–99.3%	All studied ceramics	Moderate Low-cost syringe-based printing, ink preparation, drying, and furnace processing contribute to total cost	Ink rheology dependence and moderate printing speeds make it less adapted for volume production

For DIW, particle size distribution and surface interactions must support extrusion while providing sufficient resistance to deformation after deposition. Renteria et al. [113] investigated bimodal mixtures of 100 and 400 nm $BaTiO_3$ particles and showed that particle grading affected sintering shrinkage, relative density, and piezoelectric properties. A majority of small particles (100 nm) could enhance the viscosity considerably, which can complicate the extrusion process, in contrast with a 50-50% vol bimodal particle distribution, which enabled a moderate viscosity and an enhanced packing density. Particle morphology also influences DIW feedstock behavior. Walton et al. [128] reported that the addition of 0.3–2.6 vol% of $BaTiO_3$ platelets to lead-based piezoelectric ceramic pastes caused a significant change in their rheology as a consequence of shear-induced platelet alignment. Furthermore, Lopez et al. [129] prepared textured ceramics by DIW from a mixture of spherical- and platelet-shaped $BaTiO_3$ particles and obtained the maximum degree of texture of 65%. However, increasing the platelet content from 0 to 40 wt% reduced the relative density from approximately 85.9% to 74.0%, highlighting a trade-off between texture development and densification.

Overall, SLA and DLP require a balance between flow and curing, FDM requires suitable melt behavior and filament feedability, and DIW requires extrusion followed by shape retention. For all four techniques, powder characteristics must therefore be considered together with ceramic loading and formulation chemistry.

4.2. Material Formulation and Loading Capacity

Vat photopolymerization enables relatively high ceramic loadings (30–55 vol%), although resin viscosity and light scattering pose limitations. Its dependence on photocurable monomers limits material flexibility and introduces a high organic content (~20–30 wt%), resulting in longer debinding schedules and a higher risk of piece cracking and delamination. In contrast, DIW can accommodate pastes containing >60 vol% ceramic, benefiting from a low binder content (<5 wt%) that simplifies debinding and reduces the piece's shrinkage. Moreover, alternative sintering and debinding technologies (microwave, UHS) are more compatible with DIW due to the low organic content. FDM lies between these two extremes: although filaments with 30–40 vol% ceramic are commonly printable, pushing beyond this limit compromises flexibility and feed stability, making fully dense ceramics difficult to obtain. Thus, DIW remains highly suitable for high-density ceramics, whereas SLA/DLP offers better precision, and FDM is the least ideal for ceramic loading due to filament brittleness. Nevertheless, the use of desktop FDM, where a long filament feed is not needed, makes the printing easier, even if the filament is not exceptionally flexible. Overall, in terms of ceramic loading and processability, DIW has a clear advantage here.

4.3. Print Resolution and Feature Control

Vat photopolymerization, especially stereolithography, delivers a reported resolution as fine as 10 µm [130], enabling microarchitectures, thin-walled structures, and fine lattices. Both DIW and FDM use nozzle sizes of a few hundred micrometers and exhibit a z resolution on the hundreds-of-microns scale for DIW [131], depending on the nozzle size and ink rheology, and (50–200 µm) for FDM [126,130], depending on the nozzle size. As a result, SLA/DLP are more suitable for microscale geometries, whereas FDM and DIW are better suited for meso- to macroscale components.

4.4. Rheology and Printing Constraints

DIW requires advanced rheological control: yield stress, shear thinning, and viscoelastic balance, making formulation the major challenge. SLA/DLP face optical constraints, such as refractive index mismatch and light penetration depth, which complicate doping

strategies or multimaterial systems. FDM, on the other hand, suffers primarily from filament flexibility as well as nozzle friction and stick–slip phenomena at high ceramic loadings. Therefore, each technique exhibits a different bottleneck—SLA/DLP: optical physics; DIW: rheology; FDM: filament integrity.

4.5. Porosity, Debinding, and Final Densification

SLA/DLP and FDM both contain large organic fractions, leading to multi-step debinding (chemical + thermal) that increases the risk of cracking and internal pressure buildup. DIW's low organic content significantly reduces this risk, enabling single-step debinding and sintering in some cases. Final densities of approximately 95% are achievable with these techniques. In FDM and SLA/DLP, the filaments and resins must be highly loaded (above 40 vol%) to achieve a high relative density with minimal shrinkage. Thus, the DIW technique can offer a less complex debinding step compared to vat photopolymerization and fused deposition modeling techniques.

4.6. Cost and Versatility

In terms of cost, vat photopolymerization technology can be more expensive, owing to the high costs of resins and photo-initiators, as well as to SLA or DLP equipment, which are more expensive than DIW or FDM. For this criterion, FDM can be a more cost-effective technique due to the accessibility of desktop FDM, which enables researchers to access extrusion-based technology at a relatively low cost. Similarly, DIW technology also presents cost advantages, as this technique generally depends directly on low-cost fabricated pastes without the need for high-cost photopolymerizable resins or expensive extrusion machines. Even in terms of versatility, the fact that FDM uses filaments that can be loaded with almost any type of material or doped compositions makes this technology highly versatile and cost-effective, compared to SLA/DLP, where the refractive index limits its versatility, even for doped compositions, complicating the printing of these materials.

Furthermore, as mentioned before, photopolymerization-based techniques tend to be more energy-intensive than extrusion-based methods. Among the latter, DIW is particularly energy-efficient as it operates at room temperature without the heating required by FDM.

4.7. Scalability and Industrial Maturity

FDM is one of the most mature and accessible techniques due to low equipment costs and user-friendly operation. DIW has moderate scalability but remains limited by ink stability and the need for controlled drying. Vat photopolymerization, despite offering excellent resolution for miniaturized and high-precision components, is less suited for moderate- to high-volume parts that do not necessarily need exceptional printing accuracy, reducing industrial accessibility. Therefore, industrial choices are often governed by the trade-off between precision (SLA/DLP), density (DIW), and cost/scalability (FDM).

Overall, no single technique dominates all criteria. Instead, each AM route offers specific advantages aligned to targeted applications: SLA/DLP is generally more suitable for microstructured devices and high-precision miniaturized ceramics. FDM can be advantageous for functional composite parts and low-cost prototyping. DIW can be more appropriate for dense ceramics and architectured porous structures. A significant gap in the current literature concerns cross-process optimization, where material formulation is adapted across multiple AM systems, as well as AI-driven predictive modeling of rheology, cure depth, and extrusion behavior. Addressing these gaps will significantly accelerate the rational design and deployment of ceramic additive manufacturing.

5. Conclusions and Future Perspectives

In this study, an extensive review of the key factors affecting the quality of the components printed by SLA, DLP, FDM, and DIW, as well as the associated critical process parameters, was conducted. The advantages and drawbacks of each method were discussed, and possible ways to address the current limitations were considered. Moreover, the review examined ceramic-based AM applications, identifying emerging trends and research directions that can further advance the field.

The comparative analysis shows that no single technique dominates all the considered criteria. SLA and DLP provide the highest resolution and good surface quality, making them particularly suitable for microstructured devices and high-precision ceramic components. However, these processes are affected by slurry viscosity, light scattering and absorption, curing depth, and the relatively high organic content of photocurable formulations. FDM offers accessible equipment, convenient filament handling, and good versatility for both ceramic–polymer composites and the indirect fabrication of ceramic parts. Nevertheless, high ceramic loading increases melt viscosity, nozzle friction, filament brittleness, and feeding instability. DIW can process highly loaded ceramic inks and is particularly suitable for dense or architectured porous structures, but its printing quality strongly depends on suspension stability, shear-thinning behavior, yield stress, viscoelastic recovery, and drying conditions.

Therefore, selecting the most suitable technique depends on the targeted material, geometry, and application. Vat photopolymerization is generally more appropriate when resolution and surface quality are the main requirements. FDM represents an interesting option when low equipment costs, automated filament feeding, and easy material handling are required, provided that sufficient ceramic loading and filament flexibility can be achieved. DIW is particularly attractive for highly loaded formulations and porous ceramic structures, although its ink formulation and rheological behavior must be carefully controlled. In all cases, printing accuracy alone does not determine the final performance. Particle packing, organic content, debinding, shrinkage, sintering conditions, and microstructural evolution strongly influence the final density, dimensional accuracy, and mechanical or functional properties.

Despite the considerable advances made in AM, ceramic additive manufacturing still presents significant prospects for future development. Combining artificial intelligence and machine learning could contribute to optimizing process parameters, predicting material behavior, and reducing trial-and-error experimentation, thereby saving both time and costs. However, the development of reliable predictive models requires sufficiently large and standardized datasets relating material composition, rheological or optical behavior, printing conditions, and final properties. At the same time, real-time monitoring and automation can enhance printing accuracy, detect defects during fabrication, and ensure more consistent production quality.

In addition, modeling and simulation, particularly finite element analysis, can provide valuable insights into the mechanical behavior and intended functionality of printed structures according to their geometry. These approaches can accelerate material selection and the design process while reducing the number of experimental trials. Coupling numerical simulation with experimental characterization could also improve the prediction of deformation, stress concentration, anisotropic shrinkage, and final device performance.

Another important area for future research concerns post-processing, particularly debinding and sintering, which strongly affect the final properties of ceramic parts. Rapid sintering methods, such as microwave sintering, fast firing, and ultrafast high-temperature sintering, could considerably reduce processing times while limiting excessive grain growth. Nevertheless, their effects on phase evolution, residual stresses, microstructure, and long-

term mechanical or functional performance require further investigation. This aspect is particularly important for dielectric, ferroelectric, and piezoelectric ceramics, whose properties strongly depend on composition, density, grain size, and microstructural evolution.

Furthermore, future studies should move beyond material formulation and printing feasibility by developing and evaluating complete functional devices under realistic operating conditions. Although many studies have demonstrated the successful printing of ceramic structures, fewer have investigated their long-term performance in applications such as sensing, energy harvesting, medical devices, electronics, or high-temperature systems. Establishing standardized methods for evaluating printability, density, dimensional accuracy, and functional properties would also allow more reliable comparisons between materials and processes.

Finally, this review serves as a reference and guide for AM researchers and engineers to identify the most suitable AM technique for their applications, understand the main process parameters, and address current challenges. Future progress will depend on stronger interactions between material formulation, digital design, printing technology, post-processing, and functional device development. The synergy between materials innovation, numerical modeling, real-time monitoring, and intelligent manufacturing could accelerate the development of reliable ceramic AM processes and open new possibilities in energy harvesting, biomedical devices, electronics, and high-performance ceramic components.

Author Contributions: S.S.: Writing—review and editing, Writing—original draft, Methodology, Investigation, Formal analysis, Data curation, and Conceptualization. M.A.B.A.: Validation and Visualization. M.R.: Validation and Visualization. Y.L.: Validation and Visualization. F.J.: Validation and Visualization. C.C.: Supervision, Validation and Visualization. All authors have read and agreed to the published version of the manuscript.

Funding: This research received no external funding.

Data Availability Statement: The original contributions presented in this study are included in the article. Further inquiries can be directed to the corresponding author.

Conflicts of Interest: The authors declare no conflict of interest.

Declaration of Generative AI and AI-Assisted Technologies in the Manuscript Preparation Process: The authors used OpenAI GPT-5.6 (ChatGPT Plus) for language editing and flow improvements. The authors have reviewed and edited the output and take full responsibility for the content of this publication.

References

1. Ten Kate, J.; Smit, G.; Breedveld, P. 3D-printed upper limb prostheses: A review. *Disabil. Rehabil. Assist. Technol.* **2017**, *12*, 300–314. [CrossRef] [PubMed]
2. Sheikh, Z.; Nayak, V.V.; Daood, U.; Kaur, A.; Moussa, H.; Canteenwala, A.; Michaud, P.-L.; De Fátima Balderrama, Í.; De Oliveira Sousa, E.; Tovar, N.; et al. Three-Dimensional Printing Methods for Bioceramic-Based Scaffold Fabrication for Craniomaxillofacial Bone Tissue Engineering. *J. Funct. Biomater.* **2024**, *15*, 60. [CrossRef] [PubMed]
3. Ahmed, A.; Azam, A.; Wang, Y.; Zhang, Z.; Li, N.; Jia, C.; Mushtaq, R.T.; Rehman, M.; Gueye, T.; Shahid, M.B.; et al. Additively manufactured nano-mechanical energy harvesting systems: Advancements, potential applications, challenges and future perspectives. *Nano Converg.* **2021**, *8*, 37. [CrossRef] [PubMed]
4. Gulzar, U.; Glynn, C.; O'Dwyer, C. Additive manufacturing for energy storage: Methods, designs and material selection for customizable 3D printed batteries and supercapacitors. *Curr. Opin. Electrochem.* **2020**, *20*, 46–53. [CrossRef]
5. Sathish, K.; Kumar, S.S.; Magal, R.T.; Selvaraj, V.; Narasimharaj, V.; Karthikeyan, R.; Sabarinathan, G.; Tiwari, M.; Kassa, A.E. A Comparative Study on Subtractive Manufacturing and Additive Manufacturing. *Adv. Mater. Sci. Eng.* **2022**, *2022*, 6892641. [CrossRef]
6. Agarwal, K.; Kuchipudi, S.K.; Girard, B.; Houser, M. Mechanical properties of fiber reinforced polymer composites: A comparative study of conventional and additive manufacturing methods. *J. Compos. Mater.* **2018**, *52*, 3173–3181. [CrossRef]

7. Pereira, T.; Kennedy, J.V.; Potgieter, J. A comparison of traditional manufacturing vs additive manufacturing, the best method for the job. *Procedia Manuf.* **2019**, *30*, 11–18. [CrossRef]
8. Valera-Jiménez, J.F.; Marín-Rueda, J.R.; Pérez-Flores, J.C.; Castro-García, M.; Canales-Vázquez, J. Additive Manufacturing of Functional Ceramics. In *3D Printing for Energy Applications*, 1st ed.; Tarancón, A., Esposito, V., Eds.; Wiley: Hoboken, NJ, USA, 2021; pp. 33–67. [CrossRef]
9. Bhasha, B.; Gautam, S.; Malik, P.; Jain, P. Ceramic Composites for Aerospace Applications. *Diffus. Found.* **2019**, *23*, 31–39. [CrossRef]
10. Steyer, T.E. Shaping the Future of Ceramics for Aerospace Applications. *Int. J. Appl. Ceram. Technol.* **2013**, *10*, 389–394. [CrossRef]
11. Buj-Corral, I.; Tejo-Otero, A. 3D Printing of Bioinert Oxide Ceramics for Medical Applications. *J. Funct. Biomater.* **2022**, *13*, 155. [CrossRef] [PubMed]
12. Cano, S.; Gonzalez-Gutierrez, J.; Sapkota, J.; Spoerk, M.; Arbeiter, F.; Schuschnigg, S.; Holzer, C.; Kukla, C. Additive manufacturing of zirconia parts by fused filament fabrication and solvent debinding: Selection of binder formulation. *Addit. Manuf.* **2019**, *26*, 117–128. [CrossRef]
13. Truxová, V.; Šafka, J.; Sobotka, J.; Macháček, J.; Ackermann, M. Alumina Manufactured by Fused Filament Fabrication: A Comprehensive Study of Mechanical Properties and Porosity. *Polymers* **2022**, *14*, 991. [CrossRef] [PubMed]
14. Park, J.; Lee, D.-G.; Hur, S.; Baik, J.M.; Kim, H.S.; Song, H.-C. A Review on Recent Advances in Piezoelectric Ceramic 3D Printing. *Actuators* **2023**, *12*, 177. [CrossRef]
15. Kristiawan, R.B.; Imaduddin, F.; Ariawan, D.; Ubaidillah; Arifin, Z. A review on the fused deposition modeling (FDM) 3D printing: Filament processing, materials, and printing parameters. *Open Eng.* **2021**, *11*, 639–649. [CrossRef]
16. Solomon, I.J.; Sevvel, P.; Gunasekaran, J. A review on the various processing parameters in FDM. *Mater. Today Proc.* **2021**, *37*, 509–514. [CrossRef]
17. Chaudhary, R.; Fabbri, P.; Leoni, E.; Mazzanti, F.; Akbari, R.; Antonini, C. Additive manufacturing by digital light processing: A review. *Prog. Addit. Manuf.* **2023**, *8*, 331–351. [CrossRef]
18. Gonzalez-Gutierrez, J.; Cano, S.; Schuschnigg, S.; Kukla, C.; Sapkota, J.; Holzer, C. Additive Manufacturing of Metallic and Ceramic Components by the Material Extrusion of Highly-Filled Polymers: A Review and Future Perspectives. *Materials* **2018**, *11*, 840. [CrossRef] [PubMed]
19. Chen, Z.; Li, Z.; Li, J.; Liu, C.; Lao, C.; Fu, Y.; Liu, C.; Li, Y.; Wang, P.; He, Y. 3D printing of ceramics: A review. *J. Eur. Ceram. Soc.* **2019**, *39*, 661–687. [CrossRef]
20. Taneva, I.; Uzunov, T. Influence of post-polymerization processing on the mechanical characteristics of 3D-printed occlusal splints. *J. Phys. Conf. Ser.* **2020**, *1492*, 012018. [CrossRef]
21. Riccio, C.; Civera, M.; Grimaldo Ruiz, O.; Pedullà, P.; Rodriguez Reinoso, M.; Tommasi, G.; Vollaro, M.; Burgio, V.; Surace, C. Effects of Curing on Photosensitive Resins in SLA Additive Manufacturing. *Appl. Mech.* **2021**, *2*, 942–955. [CrossRef]
22. Dietliker, K.; Baro, J. Photoinitiators. In *Handbook of Industrial Inkjet Printing*; Zapka, W., Ed.; Wiley: Hoboken, NJ, USA, 2017; pp. 59–116. [CrossRef]
23. O'Brien, A.K.; Bowman, C.N. Impact of Oxygen on Photopolymerization Kinetics and Polymer Structure. *Macromolecules* **2006**, *39*, 2501–2506. [CrossRef]
24. Sangermano, M.; Roppolo, I.; Chiappone, A. New Horizons in Cationic Photopolymerization. *Polymers* **2018**, *10*, 136. [CrossRef] [PubMed]
25. Nuyken, O.; Pask, S. Ring-Opening Polymerization—An Introductory Review. *Polymers* **2013**, *5*, 361–403. [CrossRef]
26. Sangermano, M.; Razza, N.; Crivello, J.V. Cationic UV-Curing: Technology and Applications: Cationic UV-Curing: Technology and Applications. *Macromol. Mater. Eng.* **2014**, *299*, 775–793. [CrossRef]
27. Sangermano, M. Recent Advances in Cationic Photopolymerization. *J. Photopol. Sci. Technol.* **2019**, *32*, 233–236. [CrossRef]
28. Bednarczyk, P.; Mozelewska, K.; Nowak, M.; Czech, Z. Photocurable Epoxy Acrylate Coatings Preparation by Dual Cationic and Radical Photocrosslinking. *Materials* **2021**, *14*, 4150. [CrossRef] [PubMed]
29. Nowak, D.; Ortyl, J.; Kamińska-Borek, I.; Kukuła, K.; Topa, M.; Popielarz, R. Photopolymerization of hybrid monomers. *Polym. Test.* **2017**, *64*, 313–320. [CrossRef]
30. Liu, C.-L.; Du, Q.; Zhang, C.; Wu, J.-M.; Zhang, G.; Shi, Y.-S. Fabrication and properties of $BaTiO_3$ ceramics via digital light processing for piezoelectric energy harvesters. *Addit. Manuf.* **2022**, *56*, 102940. [CrossRef]
31. He, Z.-X.; Gong, X.-T.; Liu, C.-L.; Du, Q.-P.; Wu, J.-M.; Zhang, G.-Z.; Shi, Y.-S. Preparation and properties of $(Ba_{0.85}Ca_{0.15})(Ti_{0.9}Zr_{0.1})O_3$ lead-free ceramics via vat photopolymerization. *Addit. Manuf.* **2022**, *59*, 103170. [CrossRef]
32. Liu, Y.; Zhan, L.; He, Y.; Zhang, J.; Hu, J.; Cheng, L.; Wu, Q.; Liu, S. Stereolithographical fabrication of dense Si3N4 ceramics by slurry optimization and pressure sintering. *Ceram. Int.* **2020**, *46*, 2063–2071. [CrossRef]
33. Dufaud, O.; Corbel, S. Oxygen diffusion in ceramic suspensions for stereolithography. *Chem. Eng. J.* **2003**, *92*, 55–62. [CrossRef]
34. Liu, C.-L.; Du, Q.; Wu, J.-M.; Zhang, G.; Shi, Y.-S. High piezoelectricity of 3D printed $BaTiO_{3-x}BaSnO_3$ piezoceramics via vat photopolymerization. *J. Eur. Ceram. Soc.* **2024**, *44*, 4639–4645. [CrossRef]

35. Li, X.; Su, H.; Dong, D.; Jiang, H.; Liu, Y.; Shen, Z.; Guo, Y.; Zhang, Z.; Guo, M. Selection strategy of curing depth for vat photopolymerization 3D printing of Al_2O_3 ceramics. *Addit. Manuf.* **2024**, *88*, 104240. [CrossRef]
36. Pan, M.-Z.; Chen, Y.-X.; Wu, J.-M.; Fan, G.-F.; Zhang, X.-Y.; Shi, Y.-S. Preparation and properties of $K_{0.48}Na_{0.52}NbO_3$ ceramics for bone scaffolds via digital light processing. *Ceram. Int.* **2023**, *49*, 38519–38526. [CrossRef]
37. Pan, Y.; He, H.; Xu, J.; Feinerman, A. Study of separation force in constrained surface projection stereolithography. *Rapid Prototyp. J.* **2017**, *23*, 353–361. [CrossRef]
38. Jiang, T.; Yan, B.; Jiang, M.; Xu, B.; Xu, Y.; Yu, Y.; Ma, T.; Wang, H. Enhanced Adhesion—Efficient Demolding Integration DLP 3D Printing Device. *Appl. Sci.* **2022**, *12*, 7373. [CrossRef]
39. Yang, C.-J. Optimizing Manufacturing Parameters of DLP Machine by Taguchi Method and Desirability Approach. *Machines* **2022**, *10*, 901. [CrossRef]
40. Moayedi Manizani, S.; Zamani, J.; Salehi, M.; Shayesteh, M. Investigating the Effect of Separation Speed and Image Cross-Section Geometry on The Separation Force in DLP Method using FEP and PP Polymer Membranes. *ADMT J.* **2023**, *16*, 9–17.
41. Chugunov, S.; Smirnov, A.; Kholodkova, A.; Tikhonov, A.; Dubinin, O.; Shishkovsky, I. Evaluation of Stereolithography-Based Additive Manufacturing Technology for $BaTiO_3$ Ceramics at 465 nm. *Appl. Sci.* **2022**, *12*, 412. [CrossRef]
42. Liu, C.-L.; Du, Q.; Zhou, H.; Wang, Y.; Chen, S.; Wu, J.-M.; Zhang, G.; Shi, Y.-S. Influence of polyethylene content on preparation and properties of lead zirconate titanate piezoelectric ceramics via vat photopolymerization. *Ceram. Int.* **2024**, *50*, 438–445. [CrossRef]
43. Liu, C.-L.; Du, Q.; Zhou, H.; Chen, S.; Wu, J.-M.; Zhang, G.; Shi, Y.-S. 3D printing of lead zirconate titanate piezoelectric ceramics via digital light processing (DLP). *Ceram. Int.* **2023**, *49*, 28492–28499. [CrossRef]
44. Liu, C.-L.; Du, Q.; Wu, J.-M.; Zhang, G.; Shi, Y.-S. Preparation of porous lead zirconate titanate piezoelectric ceramics via vat photopolymerization combined with burnt polymer spheres technique. *Addit. Manuf.* **2024**, *91*, 104326. [CrossRef]
45. Liu, C.-L.; Du, Q.; Wu, J.-M.; Zhang, G.; Shi, Y.-S. Novel 3D printed PZT-based piezoceramics for piezoelectric energy harvesting via digital light processing. *Chem. Eng. J.* **2024**, *492*, 152004. [CrossRef]
46. Liu, K.; Sun, Y.; Sun, H.; Du, Y.; Sun, C.; Shi, Y.; Yan, C. Effect of particle grading on the properties of photosensitive slurry and $BaTiO_3$ piezoelectric ceramic via digital light processing 3D printing. *J. Eur. Ceram. Soc.* **2023**, *43*, 3266–3274. [CrossRef]
47. Cao, M.; Wang, W.; Yang, X.; Zhu, W.; Zhu, X.; He, Y.; Chen, F.; Han, X. A dual-functional curcumin strategy for light scattering mitigation in high-fidelity DLP ceramic 3D printing. *Int. J. Extrem. Manuf.* **2026**, *8*, 055101. [CrossRef]
48. Zheng, K.; Quan, Y.; Ding, D.; Zhuang, J.; Wang, Y.; Wang, Z.; Zhao, J.; Fei, C.; Wang, L.; Zhao, T.; et al. 3D printed piezoelectric focused element for ultrasonic transducer. *Ceram. Int.* **2024**, *50*, 51863–51869. [CrossRef]
49. Zhai, D.; Zhao, L.; Zhang, Q.; Chen, C.; Chen, S.; Ju, D.; Yuan, X.; Zhou, X.; Zhang, D. Fabrication and performance optimization of BNT-based piezo-actuators via vat photopolymerization for actuating application. *Ceram. Int.* **2025**, *51*, 15322–15330. [CrossRef]
50. Chen, X.; Sun, J.; Cai, P.; Huang, J.; Liang, H.; Yuan, J.; Yu, S.; Bai, J. Enhancing precision in ceramic vat photopolymerization 3D printing through dispersant optimization. *Ceram. Int.* **2024**, *50*, 45114–45124. [CrossRef]
51. Zhao, L.; Yuan, X.; Zhou, X.; Wang, Q.; Li, J.; Xiong, X.; Zhang, Q.; Chen, C.; Chen, S.; Ju, D.; et al. Three-dimensional honeycomb structured $BaTiO_3$-based piezoelectric ceramics via texturing and vat photopolymerization. *Addit. Manuf.* **2024**, *95*, 104542. [CrossRef]
52. Du, Q.; Zhang, C.; Liu, C.-L.; Zhou, W.; Zeng, F.; Li, K.; Zou, K.; Fan, G.; Jiang, S.; Fu, Q.; et al. Highly <001>-textured $BaTiO_3$ ceramics with high piezoelectric performance prepared by vat photopolymerization. *Addit. Manuf.* **2023**, *66*, 103454. [CrossRef]
53. Ma, W.; Zheng, K.; Quan, Y.; Lian, Q.; Zhuang, J.; Qi, C.; Qi, S.; Zhang, J.; Li, H.; Liu, W.; et al. High-precision complex structured Sm-PMN-PT ceramics with large piezoelectric response manufactured by vat photopolymerization. *Addit. Manuf.* **2024**, *84*, 104116. [CrossRef]
54. Ma, W.; Zhou, X.; Gao, H.; Wang, C.; Tan, H.; Samart, C.; Wang, J.; Tran, N.-M.-A.; Yan, C.; Hu, Y.; et al. Structure-reinforced periodic porous piezoceramics for ultrahigh electromechanical response manufactured by vat photopolymerization. *Addit. Manuf.* **2024**, *93*, 104446. [CrossRef]
55. Zhao, L.; Zhang, Y.; Yan, M.; Li, J.; Xiong, X.; Roscow, J.; Zhang, D.; Bowen, C. Enhanced piezoelectric properties of additively manufactured BCZT with an oriented ceramic lamellar structure formed via vat photopolymerization. *J. Eur. Ceram. Soc.* **2025**, *45*, 116934. [CrossRef]
56. Wang, L.; Ma, Y.; Wang, K.; Ma, Y.; Wang, K.; Lu, B.; Niu, L.; Li, X. Fabrication of a pressure sensor using 3D printed light-cured piezoelectric composites. *Sens. Actuators A Phys.* **2023**, *362*, 114586. [CrossRef]
57. Li, Q.; Pan, Z.; Liang, J.; Zhang, Z.; Li, J.; Zhou, Y.; Sun, X. Ceramic composites toughened by vat photopolymerization 3D printing technology. *J. Mater. Sci. Technol.* **2023**, *146*, 42–48. [CrossRef]
58. Zeng, Y.; Chen, X.; Sun, L.; Yao, H.; Chen, J. Effect of different sintering additives type on Vat photopolymerization 3D printing of Al_2O_3 ceramics. *J. Manuf. Processes* **2022**, *83*, 414–426. [CrossRef]
59. He, Z.-X.; Mao, G.-X.; Wu, J.-M.; Zhang, G.; Shi, Y.-S. Effects of CuO additive on properties of high-performance $(Ba_{0.85}Ca_{0.15})(Ti_{0.9}Zr_{0.1})O_3$ piezoceramics obtained by vat photopolymerization. *Ceram. Int.* **2023**, *49*, 38973–38981. [CrossRef]

60. Chang, S.-M.; Hur, S.; Park, J.; Lee, D.-G.; Shin, J.; Kim, H.S.; Song, S.E.; Baik, J.M.; Kim, M.; Song, H.-C.; et al. Optimization of piezoelectric polymer composites and 3D printing parameters for flexible tactile sensors. *Addit. Manuf.* **2023**, *67*, 103470. [CrossRef]
61. Auffray, L.; Gouge, P.-A.; Hattali, L. Design of experiment analysis on tensile properties of PLA samples produced by fused filament fabrication. *Int. J. Adv. Manuf. Technol.* **2022**, *118*, 4123–4137. [CrossRef]
62. Zisopol, D.G.; Tănase, M.; Portoacă, A.I. Innovative Strategies for Technical-Economical Optimization of FDM Production. *Polymers* **2023**, *15*, 3787. [CrossRef] [PubMed]
63. Khunt, C.P.; Makhesana, M.A.; Mawandiya, B.K.; Patel, K.M. Investigations on the influence of printing parameters during processing of biocompatible polymer in Fused Deposition Modelling (FDM). *Adv. Mater. Process. Technol.* **2022**, *8*, 320–336. [CrossRef]
64. Qiu, D.; Langrana, N.A. Void eliminating toolpath for extrusion-based multi-material layered manufacturing. *Rapid Prototyp. J.* **2002**, *8*, 38–45. [CrossRef]
65. Nötzel, D.; Eickhoff, R.; Hanemann, T. Fused Filament Fabrication of Small Ceramic Components. *Materials* **2018**, *11*, 1463. [CrossRef] [PubMed]
66. Nötzel, D.; Eickhoff, R.; Pfeifer, C.; Hanemann, T. Printing of Zirconia Parts via Fused Filament Fabrication. *Materials* **2021**, *14*, 5467. [CrossRef] [PubMed]
67. Orlovská, M.; Chlup, Z.; Bača, Ľ.; Janek, M.; Kitzmantel, M. Fracture and mechanical properties of lightweight alumina ceramics prepared by fused filament fabrication. *J. Eur. Ceram. Soc.* **2020**, *40*, 4837–4843. [CrossRef]
68. Smirnov, A.; Nikitin, N.; Peretyagin, P.; Khmyrov, R.; Kuznetsova, E.; Solis Pinargote, N.W. Experimental and Statistical Modeling for Effect of Nozzle Diameter, Filling Pattern, and Layer Height of FDM-Printed Ceramic–Polymer Green Body on Biaxial Flexural Strength of Sintered Alumina Ceramic. *J. Compos. Sci.* **2023**, *7*, 381. [CrossRef]
69. Aw, Y.; Yeoh, C.; Idris, M.; Teh, P.; Hamzah, K.; Sazali, S. Effect of Printing Parameters on Tensile, Dynamic Mechanical, and Thermoelectric Properties of FDM 3D Printed CABS/ZnO Composites. *Materials* **2018**, *11*, 466. [CrossRef] [PubMed]
70. Cano, S.; Lube, T.; Huber, P.; Gallego, A.; Naranjo, J.A.; Berges, C.; Schuschnigg, S.; Herranz, G.; Kukla, C.; Holzer, C.; et al. Influence of the Infill Orientation on the Properties of Zirconia Parts Produced by Fused Filament Fabrication. *Materials* **2020**, *13*, 3158. [CrossRef] [PubMed]
71. Bhandari, S.; Manière, C.; Sedona, F.; De Bona, E.; Sglavo, V.M.; Colombo, P.; Fambri, L.; Biesuz, M.; Franchin, G. Ultra-rapid debinding and sintering of additively manufactured ceramics by ultrafast high-temperature sintering. *J. Eur. Ceram. Soc.* **2024**, *44*, 328–340. [CrossRef]
72. Sugavaneswaran, M.; Thomas, P.; Azad, A. Effect of electroplating on surface roughness and dimension of FDM parts at various build orientations. *FME Trans.* **2019**, *47*, 880–886. [CrossRef]
73. Kuo, C.-C.; Mao, R.-C. Development of a Precision Surface Polishing System for Parts Fabricated by Fused Deposition Modeling. *Mater. Manuf. Processes* **2016**, *31*, 1113–1118. [CrossRef]
74. Gajdoš, I.; Spišák, E.; Kaščák, L.; Krasinskyi, V. Surface Finish Techniques for FDM Parts. *Mater. Sci. Forum* **2015**, *818*, 45–48. [CrossRef]
75. Nguyen, T.K.; Lee, B.-K. Post-processing of FDM parts to improve surface and thermal properties. *Rapid Prototyp. J.* **2018**, *24*, 1091–1100. [CrossRef]
76. Mystiridou, E.; Patsidis, A.C.; Bouropoulos, N. Development and Characterization of 3D Printed Multifunctional Bioscaffolds Based on PLA/PCL/HAp/$BaTiO_3$ Composites. *Appl. Sci.* **2021**, *11*, 4253. [CrossRef]
77. Sikder, P.; Nagaraju, P.; Naganaboyina, H.P.S. 3D-Printed Piezoelectric Porous Bioactive Scaffolds and Clinical Ultrasonic Stimulation Can Help in Enhanced Bone Regeneration. *Bioengineering* **2022**, *9*, 679. [CrossRef] [PubMed]
78. Zhang, B.; Wang, L.; Song, P.; Pei, X.; Sun, H.; Wu, L.; Zhou, C.; Wang, K.; Fan, Y.; Zhang, X. 3D printed bone tissue regenerative PLA/HA scaffolds with comprehensive performance optimizations. *Mater. Des.* **2021**, *201*, 109490. [CrossRef]
79. Sebastian, T.; Bach, M.; Geiger, A.; Lusiola, T.; Kozielski, L.; Clemens, F. Investigation of Electromechanical Properties on 3-D Printed Piezoelectric Composite Scaffold Structures. *Materials* **2021**, *14*, 5927. [CrossRef] [PubMed]
80. Bach, M.; Sebastian, T.; Melnykowycz, M.; Lusiola, T.; Scharf, D.; Clemens, F. Additive Manufacturing of Piezoelectric 3-3 Composite Structures. In *Industrializing Additive Manufacturing—Proceedings of Additive Manufacturing in Products and Applications—AMPA2017*; Meboldt, M., Klahn, C., Eds.; Springer International Publishing: Cham, Switzerland, 2018; pp. 93–103. [CrossRef]
81. Kim, H.; Fernando, T.; Li, M.; Lin, Y.; Tseng, T.-L.B. Fabrication and characterization of 3D printed $BaTiO_3$/PVDF nanocomposites. *J. Compos. Mater.* **2018**, *52*, 197–206. [CrossRef]
82. Wu, Y.; Isakov, D.; Grant, P. Fabrication of Composite Filaments with High Dielectric Permittivity for Fused Deposition 3D Printing. *Materials* **2017**, *10*, 1218. [CrossRef] [PubMed]
83. Khatri, B.; Lappe, K.; Habedank, M.; Mueller, T.; Megnin, C.; Hanemann, T. Fused Deposition Modeling of ABS-Barium Titanate Composites: A Simple Route towards Tailored Dielectric Devices. *Polymers* **2018**, *10*, 666. [CrossRef] [PubMed]

84. Castles, F.; Isakov, D.; Lui, A.; Lei, Q.; Dancer, C.E.J.; Wang, Y.; Janurudin, J.M.; Speller, S.C.; Grovenor, C.R.M.; Grant, P.S. Microwave dielectric characterisation of 3D-printed $BaTiO_3$/ABS polymer composites. *Sci. Rep.* **2016**, *6*, 22714. [CrossRef] [PubMed]
85. Nötzel, D.; Hanemann, T. New Feedstock System for Fused Filament Fabrication of Sintered Alumina Parts. *Materials* **2020**, *13*, 4461. [CrossRef] [PubMed]
86. Hanemann, T.; Syperek, D.; Nötzel, D. 3D Printing of ABS Barium Ferrite Composites. *Materials* **2020**, *13*, 1481. [CrossRef] [PubMed]
87. Gorjan, L.; Galusca, C.; Sami, M.; Sebastian, T.; Clemens, F. Effect of stearic acid on rheological properties and printability of ethylene vinyl acetate based feedstocks for fused filament fabrication of alumina. *Addit. Manuf.* **2020**, *36*, 101391. [CrossRef]
88. Veteška, P.; Hajdúchová, Z.; Feranc, J.; Tomanová, K.; Milde, J.; Kritikos, M.; Bača, Ľ.; Janek, M. Novel composite filament usable in low-cost 3D printers for fabrication of complex ceramic shapes. *Appl. Mater. Today* **2021**, *22*, 100949. [CrossRef]
89. Choi, J.; Kim, P.J.H.; Seo, J.; Kwon, J.; Lee, S.; Song, T. Environmentally-harmless polylactic acid-polyethylene glycol binder for deformable ceramic green body. *Ceram. Int.* **2018**, *44*, 4220–4224. [CrossRef]
90. Chieng, B.W.; Ibrahim, N.A.; Yunus, W.M.Z.W.; Hussein, M.Z. Plasticized poly(lactic acid) with low molecular weight poly(ethylene glycol): Mechanical, thermal, and morphology properties. *J. Appl. Polym. Sci.* **2013**, *130*, 4576–4580. [CrossRef]
91. Goulas, A.; McGhee, J.R.; Whittaker, T.; Ossai, D.; Mistry, E.; Whittow, W.; Vaidhyanathan, B.; Reaney, I.M.; Vardaxoglou, J.C.; Engstrøm, D.S. Synthesis and dielectric characterisation of a low loss $BaSrTiO_3$/ABS ceramic/polymer composite for fused filament fabrication additive manufacturing. *Addit. Manuf.* **2022**, *55*, 102844. [CrossRef]
92. Bhandari, S.; Veteška, P.; Vajpayee, G.; Hinterstein, M.; Bača, Ľ.; Hajdúchová, Z.; Špitalský, Z.; Franchin, G.; Janek, M. Material-extrusion based additive manufacturing of $BaTiO_3$ ceramics: From filament production to sintered properties. *Addit. Manuf.* **2024**, *88*, 104238. [CrossRef]
93. Smirnov, A.; Peretyagin, P.; Nikitin, N. Assessment Effect of Nanometer-Sized Al_2O_3 Fillers in Polylactide on Fracture Probability of Filament and 3D Printed Samples by FDM. *Materials* **2023**, *16*, 1671. [CrossRef] [PubMed]
94. Smirnov, A.; Terekhina, S.; Tarasova, T.; Hattali, L.; Grigoriev, S. From the development of low-cost filament to 3D printing ceramic parts obtained by fused filament fabrication. *Int. J. Adv. Manuf. Technol.* **2023**, *128*, 511–529. [CrossRef]
95. Smirnov, A.; Seleznev, A.; Peretyagin, P.; Bentseva, E.; Pristinskiy, Y.; Kuznetsova, E.; Grigoriev, S. Rheological Characterization and Printability of Polylactide (PLA)-Alumina (Al_2O_3) Filaments for Fused Deposition Modeling (FDM). *Materials* **2022**, *15*, 8399. [CrossRef] [PubMed]
96. Heim, T.; Kern, F. Influence of the Feedstock Preparation on the Properties of Highly Filled Alumina Green-Body and Sintered Parts Produced by Fused Deposition of Ceramic. *Ceramics* **2023**, *6*, 241–254. [CrossRef]
97. Zhao, Q.; Chen, R.; Wang, S.; Hao, W.; Dong, W.; Li, X.; Wang, L. Utilization of fused deposition modeling in the fabrication of lattice structural Al_2O_3 ceramics. *Ceram. Int.* **2024**, *50*, 35193–35202. [CrossRef]
98. Franco Urquiza, E.A. Advances in Additive Manufacturing of Polymer-Fused Deposition Modeling on Textiles: From 3D Printing to Innovative 4D Printing—A Review. *Polymers* **2024**, *16*, 700. [CrossRef] [PubMed]
99. Song, R.; Zhao, Y.; Li, W.; Yu, Y.; Sheng, J.; Li, Z.; Zhang, Y.; Xia, H.; Fei, W.-D. High temperature stability and mechanical quality factor of donor-acceptor co-doped $BaTiO_3$ piezoelectrics. *Acta Mater.* **2019**, *181*, 200–206. [CrossRef]
100. Zhu, L.; Zhang, B.; Zhao, X.; Zhao, L.; Zhou, P.; Li, J. Enhanced Piezoelectric Properties of $(Ba_{1-x}Ca_x)(Ti_{0.92}Sn_{0.08})O_3$ Lead-Free Ceramics. *J. Am. Ceram. Soc.* **2013**, *96*, 241–245. [CrossRef]
101. Zhao, C.; Wu, H.; Li, F.; Cai, Y.; Zhang, Y.; Song, D.; Wu, J.; Lyu, X.; Yin, J.; Xiao, D.; et al. Practical High Piezoelectricity in Barium Titanate Ceramics Utilizing Multiphase Convergence with Broad Structural Flexibility. *J. Am. Chem. Soc.* **2018**, *140*, 15252–15260. [CrossRef] [PubMed]
102. Huang, Y.; Zhao, C.; Wu, B.; Zhang, X. Grain size effects and structure origin in high-performance $BaTiO_3$-based piezoceramics with large grains. *J. Eur. Ceram. Soc.* **2022**, *42*, 2764–2771. [CrossRef]
103. Ul, R.; Marchet, P.; Pham-Thi, M.; Tran-Huu-Hue, L.-P. Improved Properties of Doped $BaTiO_3$ Piezoelectric Ceramics. *Phys. Status Solidi A* **2019**, *216*, 1900413. [CrossRef]
104. Kimura, T.; Dong, Q.; Yin, S.; Hashimoto, T.; Sasaki, A.; Sato, T. Synthesis and piezoelectric properties of Li-doped $BaTiO_3$ by a solvothermal approach. *J. Eur. Ceram. Soc.* **2013**, *33*, 1009–1015. [CrossRef]
105. Zhu, L.-F.; Zhang, B.-P.; Yang, W.-G. Enhancing piezoelectric coefficient d33 in LiF-doped $BaTiO_3$ ceramics by optimizing excess Ba content. *Mater. Res. Bull.* **2014**, *52*, 158–161. [CrossRef]
106. Peng, E.; Zhang, D.; Ding, J. Ceramic Robocasting: Recent Achievements, Potential, and Future Developments. *Adv. Mater.* **2018**, *30*, 1802404. [CrossRef] [PubMed]
107. Franks, G.V.; Tallon, C.; Studart, A.R.; Sesso, M.L.; Leo, S. Colloidal processing: Enabling complex shaped ceramics with unique multiscale structures. *J. Am. Ceram. Soc.* **2017**, *100*, 458–490. [CrossRef]
108. Li, J.; Yan, M.; Zhang, Y.; Li, Z.; Xiao, Z.; Luo, H.; Yuan, X.; Zhang, D. Optimization of polarization direction on 3D printed 3-3 piezoelectric composites for sensing application. *Addit. Manuf.* **2022**, *58*, 103060. [CrossRef]

109. Chen, F.; Yang, C.; An, Z.; Zhang, X.; Zhou, T.; Chen, N. Direct-ink-writing of multistage-pore structured energy collector with ultrahigh ceramic content and toughness. *Mater. Des*. **2022**, *217*, 110652. [CrossRef]
110. Gadea, C.; Spelta, T.; Simonsen, S.B.; Esposito, V.; Bowen, J.R.; Haugen, A.B. Hybrid inks for 3D printing of tall $BaTiO_3$-based ceramics. *Open Ceram*. **2021**, *6*, 100110. [CrossRef]
111. Hossain, S.S.; Jang, S.; Park, S.; Bae, C.-J. Understanding ink design and printing dynamics of extrusion-based 3D printing: Defect-free dense piezoelectric ceramics. *J. Manuf. Processes* **2023**, *92*, 1–11. [CrossRef]
112. Lorenz, M.; Martin, A.; Webber, K.G.; Travitzky, N. Electromechanical Properties of Robocasted Barium Titanate Ceramics. *Adv. Eng. Mater.* **2020**, *22*, 2000325. [CrossRef]
113. Lamnini, S.; Elsayed, H.; Lakhdar, Y.; Baino, F.; Smeacetto, F.; Bernardo, E. Robocasting of advanced ceramics: Ink optimization and protocol to predict the printing parameters—A review. *Heliyon* **2022**, *8*, e10651. [CrossRef] [PubMed]
114. Renteria, A.; Garcia, L.F.; Balcorta, V.H.; Ortiz, D.; Delfin, L.C.; Regis, J.; Marcos-Hernández, M.; Espalin, D.; Tseng, T.-L.; Lin, Y. Influence of bimodal particle distribution on material properties of $BaTiO_3$ fabricated by paste extrusion 3D printing. *Ceram. Int.* **2021**, *47*, 18477–18486. [CrossRef]
115. Bhandari, S.; Hanzel, O.; Veteška, P.; Janek, M.; De Bona, E.; Sglavo, V.M.; Biesuz, M.; Franchin, G. From rapid prototyping to rapid firing: On the feasibility of high-speed production for complex $BaTiO_3$ components. *J. Am. Ceram. Soc*. **2024**, *107*, 6562–6573. [CrossRef]
116. Bhandari, S.; Hanzel, O.; Kermani, M.; Sglavo, V.M.; Biesuz, M.; Franchin, G. Rapid debinding and sintering of alumina ceramics fabricated by direct ink writing. *J. Eur. Ceram. Soc*. **2025**, *45*, 117144. [CrossRef]
117. Damamme, R.; Seveyrat, L.; Borta-Boyon, A.; Nguyen, V.-C.; Le, M.-Q.; Cottinet, P.-J. 3D printing of doped barium-titanate using robocasting—Toward new generation lead-free piezoceramic transducers. *J. Eur. Ceram. Soc*. **2023**, *43*, 3297–3306. [CrossRef]
118. Wei, X.; Liu, Y.; Zhao, D.; Ge, S.S. 3D printing of piezoelectric barium titanate with high density from milled powders. *J. Eur. Ceram. Soc*. **2020**, *40*, 5423–5430. [CrossRef]
119. Li, Y.; Li, L.; Li, B. Direct Ink Writing of Three-Dimensional (K, Na)NbO_3-Based Piezoelectric Ceramics. *Materials* **2015**, *8*, 1729–1737. [CrossRef] [PubMed]
120. Liu, K.; Zhang, Q.; Zhou, C.; Shi, Y.; Sun, C.; Sun, H.; Yin, C.; Hu, J.; Zhou, S.; Zhang, Y.; et al. 4D Printing of Lead Zirconate Titanate Piezoelectric Composites Transducer Based on Direct Ink Writing. *Front. Mater.* **2021**, *8*, 659441. [CrossRef]
121. Li, Y.-Y.; Li, L.-T.; Li, B. Direct ink writing of 3–3 piezoelectric composite. *J. Alloys Compd*. **2015**, *620*, 125–128. [CrossRef]
122. Li, J.; Zhang, Y.; Yan, M.; Zhong, C.; Zhao, L.; Zhai, D.; Luo, H.; Yuan, X.; Zhang, D. 3D printing of flexible piezoelectric composite with integrated sensing and actuation applications. *Adv. Powder Mater.* **2024**, *3*, 100226. [CrossRef]
123. Liu, K.; Hu, J.; Du, Y.; Shi, Y.; Sun, Y.; Zhang, S.; Tu, R.; Zhang, Q.; Huang, S.; Sun, H. Influence of particle size on 3D-printed piezoelectric ceramics via digital light processing with furnace sintering. *Int. J. Appl. Ceram. Technol*. **2022**, *19*, 2461–2471. [CrossRef]
124. Spirrett, F.; Ito, T.; Kirihara, S. High-Speed Alumina Stereolithography. *Appl. Sci*. **2022**, *12*, 9760. [CrossRef]
125. De Lisi, M.; Kovacev, N.; Attia, U.M.; Essa, K. Numerical Simulation of Sintering of DLP Printed Alumina Ceramics. *Aerospace* **2022**, *9*, 336. [CrossRef]
126. Wang, X.; Jiang, M.; Zhou, Z.; Gou, J.; Hui, D. 3D printing of polymer matrix composites: A review and prospective. *Compos. Part B Eng*. **2017**, *110*, 442–458. [CrossRef]
127. Gourdonnaud, D.; Pateloup, V.; Junger, A.; Bourret, J.; Chartier, T.; Geffroy, P.-M. Correlation between filament deposition path, microstructural and mechanical properties of dense alumina parts printed by robocasting. *J. Eur. Ceram. Soc*. **2024**, *44*, 1027–1035. [CrossRef]
128. Walton, R.L.; Fanton, M.A.; Meyer, R.J.; Messing, G.L. Dispersion and rheology for direct writing lead-based piezoelectric ceramic pastes with anisotropic template particles. *J. Am. Ceram. Soc*. **2020**, *103*, 6157–6168. [CrossRef]
129. Lopez, A.; Rodriguez, L.; Rodriguez, A.; Arroyo, S.; Loera, A.; Fontes, D.; Perez, S.; Mahmud, M.S.; Molina, L.; Zaman, S.; et al. Additive manufacturing of textured barium titanate ceramics via shear force-induced platelet alignment. *Int. J. Ceram. Engine Sci.* **2025**, *7*, e70003. [CrossRef]
130. Ngo, T.D.; Kashani, A.; Imbalzano, G.; Nguyen, K.T.Q.; Hui, D. Additive manufacturing (3D printing): A review of materials, methods, applications and challenges. *Compos. Part B Eng*. **2018**, *143*, 172–196. [CrossRef]
131. Thiraux, R.; Dupuy, A.D.; Ainger, K.M.; Valdevit, L. A multi-scale process for mechanical characterization of ceramic materials produced by Direct Ink Writing. *Open Ceram*. **2024**, *17*, 100544. [CrossRef]

Disclaimer/Publisher's Note: The statements, opinions and data contained in all publications are solely those of the individual author(s) and contributor(s) and not of MDPI and/or the editor(s). MDPI and/or the editor(s) disclaim responsibility for any injury to people or property resulting from any ideas, methods, instructions or products referred to in the content.